

# Swift heavy ion track formation in $\text{Gd}_2\text{Zr}_{2-x}\text{Ti}_x\text{O}_7$ pyrochlore: Effect of electronic energy loss



Maik Lang<sup>a,\*</sup>, Marcel Toulemonde<sup>b</sup>, Jiaming Zhang<sup>c</sup>, Fuxiang Zhang<sup>d</sup>, Cameron L. Tracy<sup>e</sup>, Jie Lian<sup>f</sup>, Zhongwu Wang<sup>g</sup>, William J. Weber<sup>h,i</sup>, Daniel Severin<sup>j</sup>, Markus Bender<sup>j</sup>, Christina Trautmann<sup>j,k</sup>, Rodney C. Ewing<sup>c</sup>

<sup>a</sup> Department of Nuclear Engineering, University of Tennessee, Knoxville, TN 37996, USA

<sup>b</sup> Centre interdisciplinaire de recherche sur les Ions, les Matériaux et la Photonique (CIMAP), CEA-CNRS-ENSICAEN-University of Caen, 14070 Caen, France

<sup>c</sup> Department of Geological and Environmental Science, School of Earth Science, Stanford University, Stanford 94305, USA

<sup>d</sup> Department of Earth and Environmental Sciences, University of Michigan, Ann Arbor, MI 48109, USA

<sup>e</sup> Department of Materials Science & Engineering, University of Michigan, Ann Arbor, MI 48109, USA

<sup>f</sup> Department of Mechanical, Aerospace and Nuclear Engineering, Rensselaer Polytechnic Institute, Troy, NY 12180, USA

<sup>g</sup> Cornell High Energy Synchrotron Source, Cornell University, Ithaca, NY 14853, USA

<sup>h</sup> Department of Materials Science and Technology, University of Tennessee, Knoxville, TN 37996, USA

<sup>i</sup> Materials Science and Technology Division, Oak Ridge National Laboratory, Oak Ridge, TN 37831, USA

<sup>j</sup> GSI Helmholtz Centre for Heavy Ion Research, 64291 Darmstadt, Germany

<sup>k</sup> Technische Universität Darmstadt, 64287 Darmstadt, Germany

## ARTICLE INFO

### Article history:

Received 4 February 2014

Received in revised form 16 June 2014

Accepted 20 June 2014

Available online 23 July 2014

### Keywords:

Swift heavy ions

Pyrochlore

Ceramics

Amorphization

Disordering

## ABSTRACT

The morphology of swift heavy ion tracks in the  $\text{Gd}_2\text{Zr}_{2-x}\text{Ti}_x\text{O}_7$  pyrochlore system has been investigated as a function of the variation in chemical composition and electronic energy loss,  $dE/dx$ , over a range of energetic ions:  $^{58}\text{Ni}$ ,  $^{101}\text{Ru}$ ,  $^{129}\text{Xe}$ ,  $^{181}\text{Ta}$ ,  $^{197}\text{Au}$ ,  $^{208}\text{Pb}$ , and  $^{238}\text{U}$  of 11.1 MeV/u specific energy. Bright-field transmission electron microscopy, synchrotron X-ray diffraction, and Raman spectroscopy reveal an increasing degree of amorphization with increasing Ti-content and  $dE/dx$ . The size and morphology of individual ion tracks in  $\text{Gd}_2\text{Ti}_2\text{O}_7$  were characterized by high-resolution transmission electron microscopy revealing a core-shell structure with an outer defect-fluorite dominated shell at low  $dE/dx$  to predominantly amorphous tracks at high  $dE/dx$ . Inelastic thermal-spike calculations have been used together with atomic-scale characterization of ion tracks in  $\text{Gd}_2\text{Ti}_2\text{O}_7$  by high resolution transmission electron microscopy to deduce critical energy densities for the complex core-shell morphologies induced by ions of different  $dE/dx$ .

© 2014 Elsevier B.V. All rights reserved.

## 1. Introduction

Irradiation effects of swift heavy ions in ceramic oxides, such as pyrochlore,  $\text{A}_2\text{B}_2\text{O}_7$ , have recently attracted a great deal of attention. Complex damage structures have been identified within individual ion tracks after irradiation with GeV particles, including the formation of nanoscale equilibrium and non-equilibrium phases [1–3]. A detailed description of the track-formation process is associated with two key questions: (1) How is the ion energy deposited into the electron subsystem of a nano-metric volume during extremely short time scales and how is this energy eventually transferred to the target atoms? (2) What damage recovery

processes occur during the cooling down stage leading to the final configuration of the stabilized atomic track structure? At present, it is difficult to distinguish between track formation and recovery processes as the time scales are so short; thus, there are no experimental techniques that allow one to follow the *in situ* motion of electrons and atoms during excitation and relaxation within nano-scale volumes and at femto- to picosecond time frames ( $10^{-15}$  to  $10^{-12}$  s). Thus, present understanding relies on macroscopic [4,5] and microscopic [6–9] models that have been developed to describe the formation of ion tracks.

Isometric pyrochlore ( $Fd\bar{3}m$ ,  $Z=8$ ,  $a=0.9\text{--}1.2\text{ nm}$ ) is closely related to the fluorite structure ( $\text{AX}_2$ ), with two cation sites and one-eighth fewer anions [10]. Due to their structural flexibility and diverse chemistry, pyrochlore oxides have a wide variety of properties that find application in a number of different technologies, from

\* Corresponding author. Tel.: +1 865 974 8247.

E-mail address: [mlang2@utk.edu](mailto:mlang2@utk.edu) (M. Lang).

electrolytes in solid oxide fuel cells to actinide-bearing compounds that can be used as nuclear waste forms or inert matrix nuclear fuels [11–14]. In particular, pyrochlore oxides are of great interest for ion-beam studies, as the induced structural modifications are strongly linked to the details of the bonding environment. Irradiation with low-energy ions (keV–MeV) in the nuclear collision regime triggers phase transformations, such as crystalline-to-amorphous and order-to-disorder (pyrochlore-to-defect fluorite) transitions, depending on the cation ionic radius ratio ( $r_A/r_B$ ) [12,15]. Such transitions are controlled by the accumulation of Frenkel defects or antisite defects (mixed occupancy of  $A^{3+}$  and  $B^{4+}$ ) in the cation sublattice, and by the formation of Frenkel defects on the anion sublattice [10–20]. Recently, pyrochlore has also been irradiated with swift heavy ions (GeV) in the electronic energy loss ( $dE/dx$ ) regime [21–32]. A multi-analytical approach revealed that single ion tracks in the binary  $Gd_2Zr_{2-x}Ti_xO_7$  ( $x = 0, 0.5, 1, 1.5$ , and  $2$ ) consist of three distinct, concentric damage zones: (i) an amorphous track core, (ii) a disordered shell with a defect-fluorite structure, and (iii) a distant halo of defect-rich pyrochlore [24]. This complex damage morphology provides a unique opportunity to identify possible damage recovery processes related to the quenching of ion tracks. Based on randomized energy depositions to the atomic-lattice (thermalized energy), molecular dynamics simulations have been performed in which the time evolution of individual tracks was followed, revealing the phase-transition pathways to the concentric track structures observed experimentally [1,2]. The chemical composition of the pyrochlore sample has a strong effect on the size and morphology of tracks, and the resistance to irradiation-induced amorphization significantly increases with the Zr-content in the binary  $Gd_2Zr_{2-x}Ti_xO_7$ . For the  $Gd_2Zr_2O_7$  end-member, amorphization has only been achieved for the extreme energy deposition density resulting from  $C_{60}$ -cluster irradiation [25].

The present paper focuses on structural modifications in different pyrochlore compositions ( $Gd_2Zr_{2-x}Ti_xO_7$ ) that result from a wide range of energetic ions. This allows the study of track formation as function of the electronic energy loss in a class of ceramics covering the entire spectrum from amorphizable to non-amorphizable oxide insulators. The experimental results are discussed with respect to the applied characterization techniques and existing data in the literature. A set of track diameters deduced from high resolution transmission electron microscopy observations have been used to perform calculations for track formation in  $Gd_2Ti_2O_7$  vs.  $dE/dx$  using the inelastic thermal spike model.

## 2. Experimental procedure

Polycrystalline samples of the  $Gd_2Zr_{2-x}Ti_xO_7$  binary were used where  $x = 0, 0.5, 1, 1.5$ , and  $2$  (see for details reference [25]). The starting materials were dense pellets with a typical grain size on the order of a few  $\mu m$ . The calculated densities ranged from  $6.64 \text{ g/cm}^3$  ( $Gd_2Zr_2O_7$ ) to  $6.56 \text{ g/cm}^3$  ( $Gd_2Ti_2O_7$ ). The mm-thick samples were polished (roughness:  $\leq 1 \mu m$ ) without specific orientation down to a thickness of  $\sim 40 \mu m$  and subsequently annealed at  $800^\circ C$  for 24 h to release absorbed water. For irradiation, the pellets were cut into small pieces,  $\sim 0.25 \text{ cm}^2$ . All ion-irradiation experiments were performed at the beamline X0 of the UNILAC linear accelerator at the GSI Helmholtz Center (Darmstadt Germany) using  $^{58}Ni$ ,  $^{101}Ru$ ,  $^{129}Xe$ ,  $^{181}Ta$ ,  $^{197}Au$ ,  $^{208}Pb$ , and  $^{238}U$  ions of specific energy 11.1 MeV/u (atomic mass unit u) at room temperature and under normal incidence. The total kinetic energy and the electronic  $dE/dx$  of all ions according to the SRIM-2008 code [33] are listed in Table 1. The ion-beam flux was limited to  $\sim 10^8 \text{ ions/cm}^2 \text{ s}$ , which is sufficiently low to avoid noticeable sample heating. The projected range of all the ions was greater than the sample thickness. Thus, the ions completely passed through the specimens depositing an almost constant electronic energy loss along their trajectory,

which was in the case of lead almost a factor of 4 larger than for nickel (Table 1, Fig. 1) [33]. The nuclear energy loss is, for all ions, assumed to be negligible because it is approximately three orders of magnitude lower than the electronic energy loss. Samples were irradiated to fluences ( $\Phi$ ) between  $5 \times 10^9$  and  $2 \times 10^{14} \text{ ions/cm}^2$  with an estimated uncertainty of 10–20%. Since a set of pyrochlore compositions was irradiated for a given ion species together on one holder and at the same ion-beam settings, the relative fluence uncertainty within a sample series should be less.

All irradiated samples were characterized by a combined analytical approach that included synchrotron X-ray diffraction (XRD), Raman spectroscopy, and transmission electron microscopy (TEM). The TEM measurements were performed with a JEOL 2010F instrument providing both bright-field and high-resolution images (HRTEM), as well as selected area electron diffraction patterns (SAED). Samples for TEM examination were prepared either by crushing the irradiated crystals into a fine powder or by conventional TEM-specimen preparation, including polishing and ion milling. This allowed the imaging of damage tracks in plain view or in cross-sectional view, depending on the relative directions of the electron beam and ion tracks. The irradiation fluence for the TEM samples was typically limited to  $\Phi \leq 1 \times 10^{11} \text{ ions/cm}^2$  in order to image non-overlapping, individual ion tracks.

Angle-dispersive synchrotron powder XRD measurements were performed at the beam line B2 of the Cornell High Energy Synchrotron Source (CHESS) of Cornell University. A mono-energetic beam of 25 keV ( $\lambda = 0.496 \text{ \AA}$ ) with spot size of  $\sim 0.5 \text{ mm}$  was used in transmission mode to analyze ion-induced structural modifications throughout the entire sample thickness. The measuring times were optimized to gain sufficient signal-to-noise ratios for data analysis and, thus, varied from sample to sample. Debye diffraction rings were recorded with a Mar CCD detector, and integrated two-dimensional patterns were produced with the software Fit 2d [34]. In order to compare data from different samples and irradiation experiments, the intensity of each pattern was normalized to the same (strongest) diffraction maximum. The amorphous fraction of each sample was deduced by deconvoluting the XRD patterns into individual crystalline and amorphous contributions and subsequent peak-fitting using the software DatLab (details of this procedure are described in an earlier study [23]).

Raman spectra were recorded in backscattering geometry using a HORIBA Jobin Yvon (HR800) micro-Raman spectrometer with a 20 mW HeNe-Laser as excitation source ( $\lambda = 632.82 \text{ nm}$ ). The Raman signal was collected from a spot diameter of  $\sim 2 \mu m$  on the polished sample surface. The measuring times varied from sample to sample and were optimized to gain sufficient signal-to-noise ratios for data analysis similar to the procedure applied for the XRD measurements. In order to compare the data of different samples and irradiation experiments, the intensity of each spectrum was normalized to the same (strongest) vibration mode. The Raman data were processed with the HORIBA Jobin Yvon software package LabSpec.

## 3. Results and discussion

### 3.1. Structural modifications in $Gd_2Zr_{2-x}Ti_xO_7$ : effect of composition and energy loss

#### 3.1.1. Transmission electron microscopy

Previous ion-beam studies revealed that individual tracks in  $Gd_2Zr_{2-x}Ti_xO_7$  pyrochlore produced by swift heavy ions exhibit concentric zones of crystalline and amorphous domains [1,2,24,29,30]. The amorphous track core is surrounded by a disordered, defect-fluorite structured shell (Fig. 2a–c). The relative amount of defect-fluorite/amorphous structure strongly increases with the Zr-content. No amorphous phase is observed for  $Gd_2Zr_2O_7$ ,

**Table 1**

Ion-beam parameters and deduced track data for irradiation experiments with  $\text{Gd}_2\text{Zr}_{2-x}\text{Ti}_x\text{O}_7$  pyrochlore samples ( $x = 0, 0.5, 1, 1.5$ , and  $2$ ) and  $^{58}\text{Ni}$ ,  $^{101}\text{Ru}$ ,  $^{129}\text{Xe}$ ,  $^{181}\text{Ta}$ ,  $^{197}\text{Au}$ ,  $^{208}\text{Pb}$ , and  $^{238}\text{U}$  ions. The electronic energy loss,  $dE/dx$ , represents the average value along the ion path within the 40- $\mu\text{m}$  thick samples (Fig. 1) according to the SRIM-2008 code [33]. The mean diameter values and uncertainties for XRD measurements were obtained from the corresponding damage cross-sections of growing amorphous sample fractions with irradiation fluence (Fig. 4). Bright-field TEM diameters (Fig. 3) represent mean values for 20 individual tracks from cross-sectional images (Fig. 2d–f). High-resolution TEM diameters of track cores (amorphous) and core + shell (amorphous + defect-fluorite) in  $\text{Gd}_2\text{Ti}_2\text{O}_7$  obtained from planar-view images.

|                                                   | $^{58}\text{Ni}$                        | $^{101}\text{Ru}$ | $^{129}\text{Xe}$ | $^{181}\text{Ta}$ | $^{197}\text{Au}$ | $^{208}\text{Pb}$ | $^{238}\text{U}$ |
|---------------------------------------------------|-----------------------------------------|-------------------|-------------------|-------------------|-------------------|-------------------|------------------|
| Energy (MeV)                                      | 644                                     | 1121              | 1432              | 2009              | 2187              | 2309              | 2642             |
| $dE/dx$ [33] (keV/nm)                             | $10.9 \pm 1.7$                          | $21.7 \pm 2.0$    | $28.5 \pm 1.5$    | $37.0 \pm 1.1$    | $40.1 \pm 1.3$    | $42.2 \pm 0.9$    | $49.7 \pm 3.9$   |
| $\text{Gd}_2\text{Zr}_{2-x}\text{Ti}_x\text{O}_7$ | XRD track diameter (nm)                 |                   |                   |                   |                   |                   |                  |
| $x = 2.0$                                         | –                                       | –                 | $4.6 \pm 0.7$     | –                 | –                 | –                 | –                |
| $x = 1.5$                                         | –                                       | –                 | $4.1 \pm 0.4$     | –                 | –                 | $7.3 \pm 0.8$     | –                |
| $x = 1.0$                                         | –                                       | –                 | $3.6 \pm 0.2$     | –                 | –                 | $6.5 \pm 0.5$     | –                |
| $x = 0.5$                                         | –                                       | –                 | $2.1 \pm 0.1$     | –                 | –                 | $5.8 \pm 1.0$     | –                |
| $x = 0.0$                                         | –                                       | –                 | 0                 | –                 | –                 | 0                 | –                |
|                                                   | Bright-field TEM track diameter (nm)    |                   |                   |                   |                   |                   |                  |
| $x = 2.0$                                         | $\leq 2.0$                              | $5.0 \pm 0.3$     | $9.2 \pm 0.9$     | $9.7 \pm 0.5$     | $10.0 \pm 0.8$    | –                 | –                |
| $x = 1.5$                                         | n.d.                                    | –                 | $6.8 \pm 0.6$     | –                 | –                 | $9.1 \pm 0.7$     | –                |
| $x = 1.0$                                         | n.d.                                    | –                 | $5.4 \pm 0.4$     | –                 | $8.3 \pm 0.2$     | $7.9 \pm 0.6$     | –                |
| $x = 0.5$                                         | n.d.                                    | –                 | $4.6 \pm 0.7$     | –                 | –                 | $6.3 \pm 0.5$     | –                |
| $x = 0.0$                                         | n.d.                                    | –                 | $3.5 \pm 0.4$     | –                 | $5.0 \pm 0.1$     | $5.6 \pm 0.3$     | $6.0 \pm 1.0$    |
| $\text{Gd}_2\text{Ti}_2\text{O}_7$                | High-resolution TEM track diameter (nm) |                   |                   |                   |                   |                   |                  |
| Core                                              | 0                                       | 1.6               | 3.2               | 6.8               | 8.6               | –                 | –                |
| Core + shell                                      | $\leq 2.0$                              | 4.8               | 7.3               | 9.5               | 11.0              | –                 | –                |

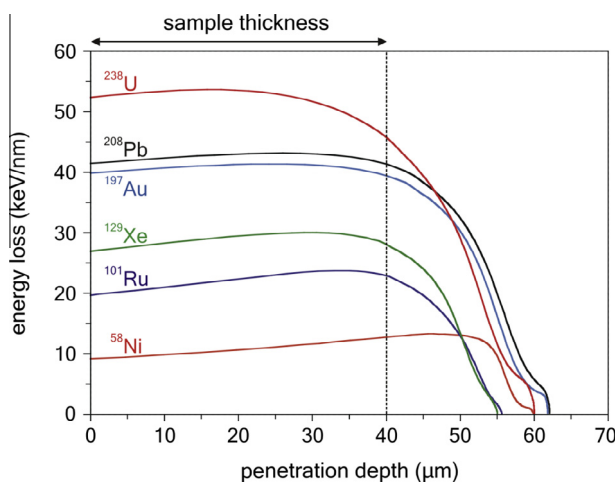


**Fig. 1.** Electronic energy loss of  $^{58}\text{Ni}$ ,  $^{101}\text{Ru}$ ,  $^{129}\text{Xe}$ ,  $^{197}\text{Au}$ ,  $^{208}\text{Pb}$ , and  $^{238}\text{U}$  ions in  $\text{Gd}_2\text{Zr}_2\text{O}_7$  pyrochlore as function of penetration depth calculated with the SRIM-2008 code [33] (for sake of clarity, data of  $^{181}\text{Ta}$  ions are omitted). All ions penetrated completely the 40- $\mu\text{m}$  thick samples and produced an almost constant energy loss over the entire thickness (Table 1).

underlining the exceptional radiation tolerance of this Zr-endmember pyrochlore. Both the amorphous phase and the defect-fluorite structure contribute to the change of contrast in cross-sectional bright-field images; however, tracks are less distinct for increasing Zr-content (Fig. 2d–f) [24,30]. No apparent electron-beam induced track annealing was detected during TEM measurements. Cylindrical damage tracks have been observed by TEM after irradiation with 1.43-GeV Xe ions for the entire pyrochlore solid solution series from  $\text{Gd}_2\text{Ti}_2\text{O}_7$  to  $\text{Gd}_2\text{Zr}_2\text{O}_7$ , for which amorphization and formation of defect fluorite are the dominant modifications, respectively [24,30]. The distance of the parallel boundaries between the region of modified contrast and the unchanged matrix in the TEM bright-field images for Au and Pb ions (Fig. 2d–f) was used in this study as a measure of the overall track diameter, i.e., comprising the core and the outer shell. For a given pyrochlore composition, about 20 individual tracks were analyzed. The mean diameters and standard deviations are summarized together with earlier data in Table 1. For the  $\text{Gd}_2\text{Zr}_{2-x}\text{Ti}_x\text{O}_7$  binary system, it was previously shown by

TEM that the track diameter in pyrochlore increases in a linear manner with the ionic radius ratio of the A- and B-site cations,  $r_A/r_B$  [24]. The track size of Au and Pb ions of high  $dE/dx$  follows the same linear trend with increasing Ti-content as compared with Xe ions of medium  $dE/dx$  (Fig. 3). The rate of diameter increase vs.  $r_A/r_B$  is, within the experimental error, identical for the different ion beams; the larger  $dE/dx$  of Au and Pb ions leads to an overall track-diameter increase of  $\sim 2$  nm over the entire compositional range (vertical off-set of the two straight lines).

### 3.1.2. Synchrotron X-ray diffraction

Comparison of synchrotron XRD patterns for a given pyrochlore composition after irradiation to the same fluence with different ions reveals the distinct effect of  $dE/dx$  on the structural response of the target material (Fig. 4a). Irradiation-induced amorphization of pyrochlore is apparent by the diffuse scattering at  $2\theta \sim 9$  and  $2\theta = 12$ – $20$  degrees, concurrent with an intensity reduction of all sharp crystalline diffraction maxima. The amorphous sample fraction grows significantly for  $\text{Gd}_2\text{Zr}_{0.5}\text{Ti}_{1.5}\text{O}_7$  irradiated to  $5 \times 10^{12}$  ions/ $\text{cm}^2$  if the ion energy loss increases from 11 keV/nm (Ni) to 29 keV/nm (Xe) and 42 keV/nm (Pb) (Fig. 4a, bottom to top patterns). The absence of crystalline diffraction maxima evidences complete amorphization in the case of the heavier Pb ions; in clear contrast, the lighter Ni ions do not cause any apparent irradiation effect. For the intermediate Xe ions, the sample contains both crystalline and amorphous regions, of roughly equal proportion [24]. A measure of the amorphous sample fraction in each sample after irradiation was obtained by coupled deconvolution and fitting of diffraction maxima. This analytical procedure, which is described in detail elsewhere [23], is based on the relative integrated intensities of the amorphous and crystalline peaks over a measured  $2\theta$  range. Thus, the ratio of the amorphous-to-crystalline fraction does not depend on X-ray beam intensity, exposure time, and sample properties (e.g., thickness and density). This approach is essential for the applied synchrotron-based XRD measurements using transmitting X-rays and pressed powders, as variations in sample thickness and density affect the overall peak intensities. An alternative method was applied by Sattonnay et al. [27,30] for the quantitative description of irradiation-induced amorphization in the same pyrochlore system. To deduce the amorphous sample fraction, they analyzed the decrease of integrated intensities of crystalline



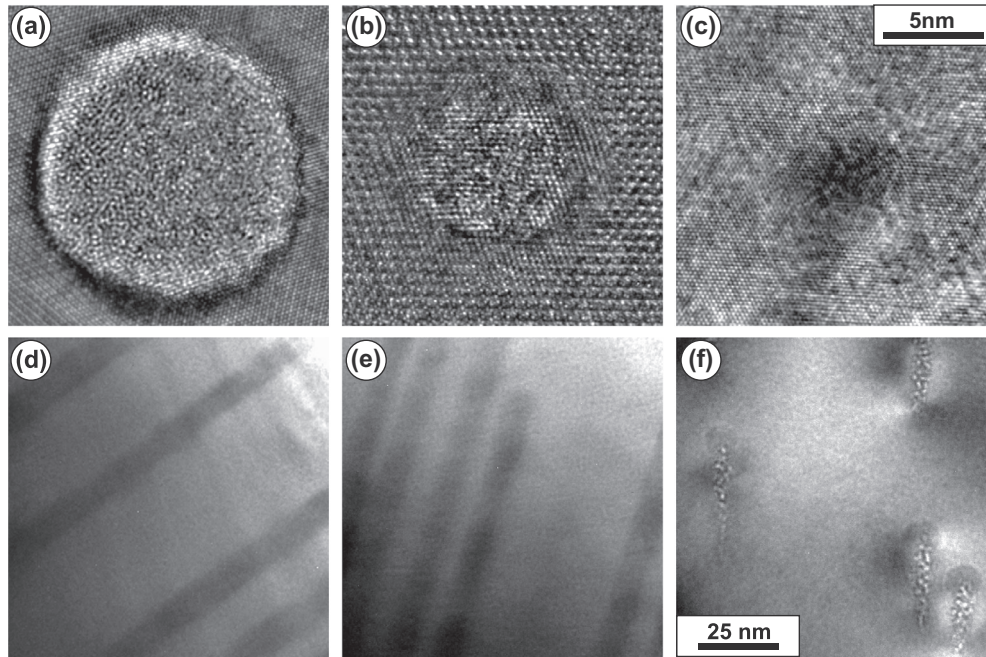


**Fig. 2.** High-resolution planar view TEM images of the morphology of individual ion tracks produced by 2.2 GeV Au ions (40.1 keV/nm) in (a)  $\text{Gd}_2\text{Zr}_2\text{O}_7$ , (b)  $\text{Gd}_2\text{TiZrO}_7$ , and (c)  $\text{Gd}_2\text{Ti}_2\text{O}_7$ . The damage morphology of swift heavy ion tracks in (a)  $\text{Gd}_2\text{Zr}_2\text{O}_7$  is complex and consists of an amorphous core surrounded by a defect-fluorite structured shell. With increasing Zr-content, (a–c), the amount of amorphous phase and the overall track size is reduced. Bright-field cross-sectional TEM images of the same pyrochlore composition irradiated with (d) 2.2 GeV Au and (e,f) 2.3 GeV Pb ions of similar  $dE/dx$  display a decreasing track contrast and size with Zr-content. The scale bar “5 nm” applies to (a–c) and the scale bar “25 nm” applies to (d–f). The TEM images (a–c) are a modified figure from [1].

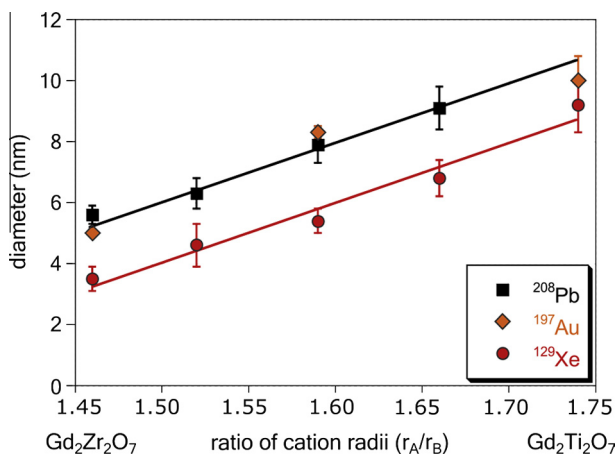


**Fig. 3.** Track diameters for three different ions directly measured from bright-field TEM images (e.g., 2d–f) as function of the ratio of the ionic radii of A (Gd) and B (Zr and/or Ti),  $r_A/r_B$ , in the  $\text{Gd}_2\text{Zr}_{2-x}\text{Ti}_x\text{O}_7$  binary system. The mean diameters increase linearly with  $r_A/r_B$  and tracks are  $\sim 2$ – $3$  nm larger for Au and Pb ions (40.1 keV/nm and 42.2 keV/nm, respectively) as compared with Xe ions (28.5 keV/nm). The errors represent sigma of 20 individual measurements. The lines are guides to the eye.

diffraction maxima from laboratory XRD patterns. This approach has the advantage that a decrease in peak intensity related to the initial crystalline phase is detectable at lower fluences, as only changes to the intense and sharp crystalline peaks are analyzed (i.e., without considering the diffuse, weakly scattering amorphous peaks). Adversely, the amorphous fraction is not determined directly, which may lead to an overestimation of the amorphization process by additional contributions to peak-intensity reductions from, e.g., the formation of the defect-fluorite structure, strain, and defects [35]. Due to the above mentioned small variations in thickness and density of synchrotron samples, this approach was not applied in this study.

A crystalline-to-amorphous transformation was not observed by XRD analysis of gadolinium zirconate pyrochlore, even for the highest electronic energy loss ions, which is in agreement with other irradiation studies [23–25,30]. This highly resistant pyrochlore oxide has been found to undergo amorphization only via the extreme energy density induced by irradiation with  $\text{C}_{60}$ -clusters [25]. In contrast, all Ti-containing pyrochlore samples showed evidence of amorphization in their XRD patterns after irradiation with Xe and Pb ions above a critical fluence. The amorphization efficiency becomes significantly greater with increasing Ti-content (for a given  $dE/dx$ ) and with the energy loss of the ions (for a given pyrochlore composition). A quantitative analysis of XRD patterns following the procedure described in [23] yielded an increasing amorphous sample fraction as a function of fluence with an initial linear behavior that reaches saturation at higher fluences (not shown here). This trend can be described by an exponential equation based on a direct-impact model [36]. Fitting of this model to the XRD data allowed for the determination of the amorphous cross-section per incident ion,  $\sigma$ , and the corresponding track diameter,  $d$ , by assuming cylindrical track symmetry and continuous damage morphology:  $\sigma = \pi (d/2)^2$  [23]. This diameter of the amorphous track core increases gradually with increasing  $r_A/r_B$  for Xe and Pb ions (Fig. 4b and Table 1). Similar to the results from TEM bright-field images, the mean XRD diameter increase is linear with the Ti-content of the pyrochlore and has comparable slopes for medium and high  $dE/dx$  ions. Ion tracks induced by Pb ions are about 3.5 nm larger in diameter as compared with tracks induced by Xe ions, reflecting the distinct increase of amorphization in all Ti-containing samples for higher  $dE/dx$  ions (Fig. 4a). Due to its unique radiation response,  $\text{Gd}_2\text{Zr}_2\text{O}_7$  is not included in the comparison of amorphous cross-sections (Fig. 4b) but is considered a singularity in terms of amorphization. Irradiation with Ni ions did not yield any detectable amorphization by means of XRD in all pyrochlore samples up to the maximum fluence; however, only the  $\text{Gd}_2\text{Ti}_2\text{O}_7$  endmember showed evidence of a small fraction of amorphous phase after irradiation to at least  $5 \times 10^{12} \text{ cm}^{-2}$  leading

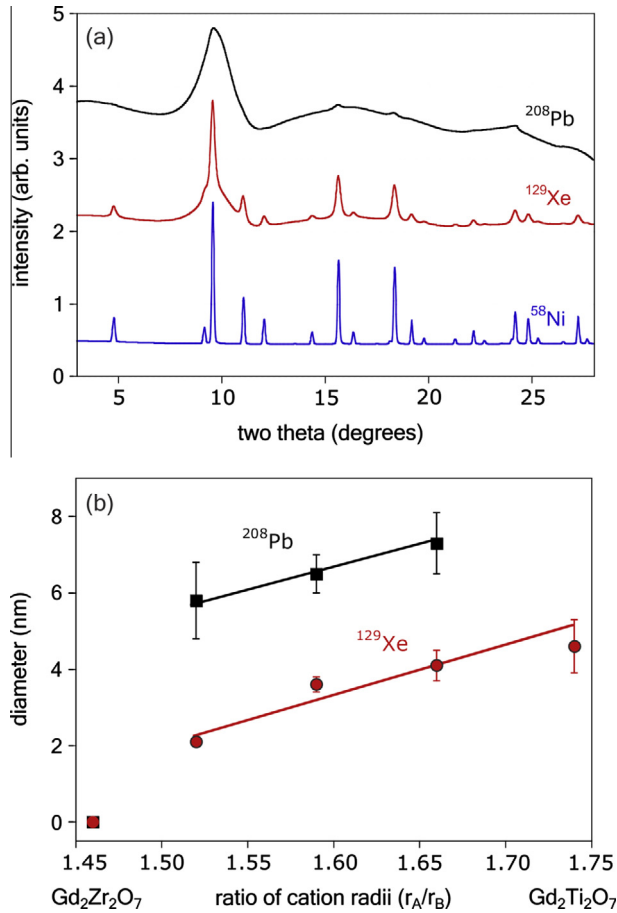


**Fig. 4.** (a) Synchrotron XRD patterns of  $\text{Gd}_2\text{Zr}_{0.5}\text{Ti}_{1.5}\text{O}_7$  pyrochlore after irradiation with Ni (10.9 keV/nm), Xe (28.5 keV/nm), and Pb (42.2 keV/nm) ions of fluence  $5 \times 10^{12} \text{ cm}^{-2}$ . The two broad peaks from amorphous domains increasingly dominate the patterns with increasing energy loss (bottom to top). (b) Mean diameter of amorphous track cores and uncertainties from peak-fitting procedure of XRD patterns [23,24] as function of the ionic radius ratio,  $r_A/r_B$ . The mean diameters increase linearly with  $r_A/r_B$  and tracks are systematically  $\sim 2\text{--}3$  nm larger for higher energy losses (Xe vs. Pb ions). XRD patterns of all samples remained unchanged after irradiation with Ni ions, except for  $\text{Gd}_2\text{Ti}_2\text{O}_7$  pyrochlore irradiated with a fluence of  $\geq 5 \times 10^{12} \text{ cm}^{-2}$  showed some evidence of amorphization (see Fig. 9).

to complete amorphization at the maximum Ni ion fluence of  $2 \times 10^{14} \text{ cm}^{-2}$ , which is further discussed in Section 3.2.

### 3.1.3. Raman spectroscopy

Raman characterization of  $\text{Gd}_2\text{Zr}_{2-x}\text{Ti}_x\text{O}_7$  samples before (Fig. 5a) and after irradiation with Pb ions (Fig. 5b) shows the strong influence of the chemical composition on the irradiation response of pyrochlore. The Raman spectrum of  $\text{A}_2\text{B}_2\text{O}_7$  pyrochlore is in general complex with six active, relatively broad vibrational modes that partly overlap. The assignment of different modes in the  $\text{Gd}_2\text{Zr}_{2-x}\text{Ti}_x\text{O}_7$  binary system and their behavior under ion irradiation have been reported in detail elsewhere [27,37,38]. The most prominent bands are the O–Gd–O bending mode ( $\sim 310 \text{ cm}^{-1}$ ) and the Gd–O stretching mode ( $\sim 515 \text{ cm}^{-1}$ ). However, details of the vibrational spectrum, such as relative peak intensities, depend on the pyrochlore composition (Fig. 5a). With increasing fluence under Pb ion irradiation (not shown here), all peaks decrease in intensity and broaden, which is in agreement to previous studies [23,24,37]. The rate of intensity reduction, e.g., for the O–Gd–O bending mode, is systematically higher for increasing Ti-content. At the maximum fluence of  $5 \times 10^{12} \text{ ions/cm}^2$ , most of the crystalline vibration modes are no longer detectable, and a broad peak-like structure at a Raman shift close to the original O–Gd–O bending mode remains for all

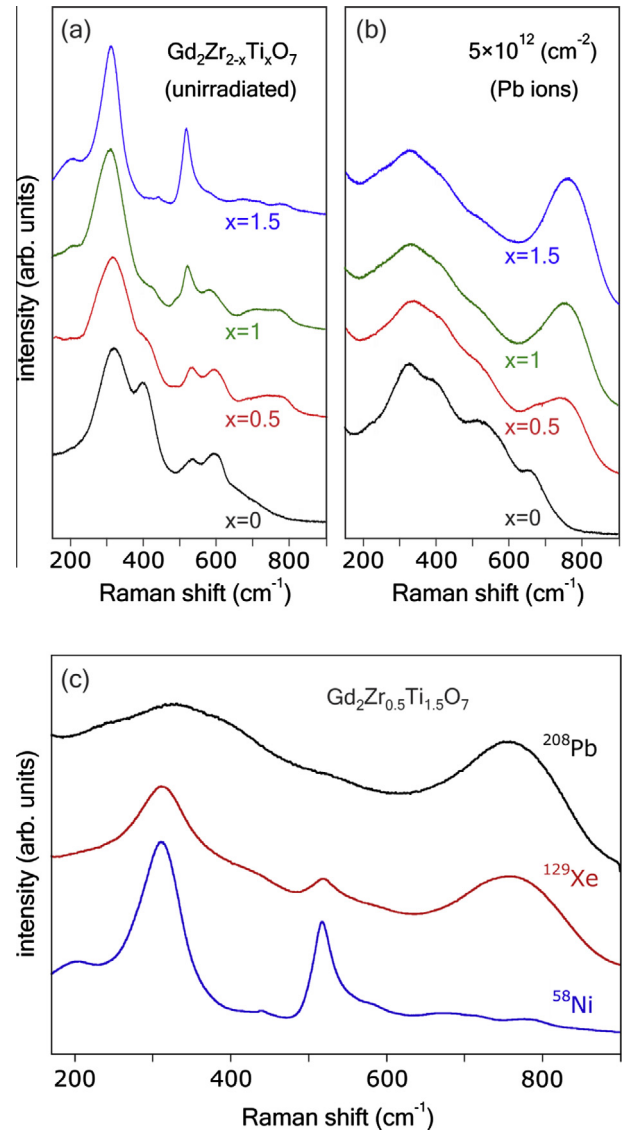


**Fig. 5.** Raman spectra of  $\text{Gd}_2\text{Zr}_{2-x}\text{Ti}_x\text{O}_7$  pyrochlore samples ( $x = 0, 0.5, 1$ , and  $1.5$ ) recorded (a) before and (b) after irradiation with Pb ions of fluence  $5 \times 10^{12} \text{ cm}^{-2}$ . (c) Raman spectra of  $\text{Gd}_2\text{Zr}_{0.5}\text{Ti}_{1.5}\text{O}_7$  pyrochlore after irradiation with Ni (10.9 keV/nm), Xe (28.5 keV/nm), and Pb (42.2 keV/nm) ions to a fluence of  $5 \times 10^{12} \text{ cm}^{-2}$ . The peak intensity of crystalline vibrational modes is reduced after irradiation accompanied by the growth of a new broad peak (at  $\sim 750 \text{ cm}^{-1}$ ) associated with the amorphous volume. The loss of pyrochlore vibrational modes and appearance of the  $\sim 750 \text{ cm}^{-1}$  maximum is larger (bottom to top) for (b) higher Ti-content and (c) increasing energy loss. The Raman spectra remained unchanged after irradiation with Ni ions up to  $1 \times 10^{13} \text{ cm}^{-2}$ .

compositions (Fig. 5b). This band has been observed in previous ion-beam experiments [23,24] and may be related to the amorphous phase and/or highly distorted, defect-rich crystalline domains. The reduction of Raman bands after irradiation is accompanied by the growth of a distinct maximum at  $\sim 750 \text{ cm}^{-1}$ . At present, there is no direct evidence that this band is uniquely related to the amorphous phase. However, the  $\sim 750 \text{ cm}^{-1}$  peak is absent in  $\text{Gd}_2\text{Zr}_2\text{O}_7$  pyrochlore and increasingly dominates the Raman spectrum with increasing Ti-content (Fig. 5b, bottom to top), in agreement with a growing amorphous track diameter with  $r_A/r_B$  as measured by XRD (Fig. 4b).

Similar to the XRD results described above, the Raman spectra of  $\text{Gd}_2\text{Zr}_{0.5}\text{Ti}_{1.5}\text{O}_7$  pyrochlore irradiated with different ions to the same fluence (Fig. 5c) also reveals the noticeable effect of  $dE/dx$ . For a fluence of  $5 \times 10^{12} \text{ ions/cm}^2$ , the absence of all crystalline

vibration modes and the dominant broad band at  $\sim 750\text{ cm}^{-1}$  indicate complete amorphization by Pb ions and partial amorphization (i.e., coexisting crystalline and amorphous sample regions) by Xe ions (Fig. 5c). In agreement with the XRD data, Ni ions do not induce any apparent irradiation effect in the Raman spectra after irradiation up to  $1 \times 10^{13}$  ions/cm<sup>2</sup> except for Gd<sub>2</sub>Ti<sub>2</sub>O<sub>7</sub>, which appears to be fully amorphous at the maximum fluence of  $2 \times 10^{14}$  ions/cm<sup>2</sup> (see Section 3.2.). A quantitative analysis of the Raman data similar to that of the XRD results for different ions and sample compositions was not completed. The composition-dependent variations in spectra prior to irradiation (Fig. 5a) and the pronounced increase of background after irradiation (Fig. 5b) did not allow for a reliable deconvolution and peak-fitting procedure, thus preventing a precise determination of damage cross-sections by Raman spectroscopy [27].

### 3.1.4. Damage cross sections and track diameters

All three complementary techniques used in this study show a consistent trend in the response of Gd<sub>2</sub>Zr<sub>2-x</sub>Ti<sub>x</sub>O<sub>7</sub> to swift heavy ion irradiation. Both the chemical composition and dE/dx significantly affect the track morphology in pyrochlore. Raman spectroscopy (Fig. 5c) and XRD measurements (Fig. 4a) independently demonstrate that amorphization increases with dE/dx for a given composition. On the other hand, for the same ion, the amorphization process is more efficient in pyrochlore samples with higher Ti-content (Figs. 4b and 5b). The absence of amorphization in the case of Ni irradiation of up to  $5 \times 10^{12}$  ions/cm<sup>2</sup> indicates the existence of a dE/dx-threshold for the direct crystalline-to-amorphous transformation within single tracks. We will show in Section 3.2. that overlapping nm-sized damage domains induced by Ni ions will lead eventually to amorphization in Gd<sub>2</sub>Ti<sub>2</sub>O<sub>7</sub> pyrochlore at very high fluences.

Direct measurements of track diameters from TEM bright-field images (Fig. 3) and diameters deduced from damage cross-sections obtained from fitting fluence-dependent XRD data (Fig. 4b) reveal a clear dependence of track size on pyrochlore composition and dE/dx. Fig. 6 compares all diameter results from both techniques showing that the average track diameter increases linearly with growing Ti content from Gd<sub>2</sub>Zr<sub>2</sub>O<sub>7</sub> to Gd<sub>2</sub>Ti<sub>2</sub>O<sub>7</sub>. Qualitatively, this is in good agreement with the reduced irradiation stability in the system Gd<sub>2</sub>Zr<sub>2-x</sub>Ti<sub>x</sub>O<sub>7</sub> for Ti-rich compositions reported earlier for MeV ions [11,37,38]. In contrast, a recent study by Sattonnay et al. suggested only a weak influence of the chemical composition on the overall

size of tracks induced by 120-MeV uranium ions [30] which might be related to the velocity effect [4]. In the present study, the mean diameter increases linearly with  $r_A/r_B$  for data from bright-field images and XRD patterns with a slope,  $m$ , that is, within the error bars, identical among each technique. Since the same analytical procedure was applied for all irradiation experiments, relative changes in track diameter are a reliable measure for the effect of dE/dx. The increase of dE/dx from 28.5 keV/nm (Xe ions) to  $\sim 41$  keV/nm (Pb and Au ions) leads to the same track-diameter increase of about 2–3 nm for each pyrochlore compositions, which is indicated by the line offset for different ions for TEM and XRD measurements, respectively (Fig. 6). The response of pyrochlore to swift heavy ion irradiation – increased track diameter for higher dE/dx ions, and the existence of a critical dE/dx-threshold for track formation – follows a general trend found for many other materials, such as for example the well-studied yttrium iron garnet (Y<sub>3</sub>Fe<sub>5</sub>O<sub>12</sub>) [39].

Similar to the results presented in Fig. 6, previous swift heavy ion investigations have applied cross-section data deduced from Raman and XRD measurements together with diameters from TEM characterization to describe quantitatively track formation in the Gd<sub>2</sub>Zr<sub>2-x</sub>Ti<sub>x</sub>O<sub>7</sub> system [24,27]. Different procedures of peak fitting and data reduction for XRD patterns and Raman spectra have been critically discussed in order to explain deviating track diameters among different authors and techniques [27]. However, as a consequence of the complex damage morphology in pyrochlore (Fig. 2), each analytical technique is limited in its ability to provide meaningful diameter results that contribute to describing accurately the track-formation process. The detailed comparison of XRD and bright-field TEM diameters in Fig. 6 highlights the limitation of a quantitative analysis and reliable interpretation of track-formation. Diameters determined by bright-field TEM images are believed to represent the entire track consisting of the amorphous core and the disordered, defect-fluorite shell (Fig. 2). This conclusion is based on the fact that both phases contribute to modifications in the observed TEM contrast with respect to the original pyrochlore matrix [24]. This assumption is further supported by a systematic larger TEM diameter for a given composition and dE/dx as compared with the corresponding XRD diameter (Fig. 6). The diameter from XRD measurements is associated with the amorphous track core due to the treatment of XRD patterns, focusing on the analysis of growing amorphous XRD maxima with the increase of irradiation. Despite the expected compositional evolution of both XRD and TEM data, the relative diameter increase with  $r_A/r_B$  is not consistent (Fig. 6). For a given energy loss, the diameters from TEM measurements increase at a higher rate ( $m \sim 19$ ) as compared with the diameters from XRD analysis ( $m \sim 11$ ). This behavior would imply that the thickness of the fluorite-structured shell, which is half of the total track diameter (TEM) minus the diameter of the amorphous core (XRD), becomes larger for more Ti-rich compositions. This is in clear contrast to experimental results obtained by high-resolution TEM (Fig. 2) showing a decreasing fluorite shell with a dominant amorphous structure with increasing Ti-content. Thus, the diameter data obtained directly from bright-field TEM images and/ or indirectly from XRD patterns are not able to fully describe the complex track morphology as revealed by high-resolution TEM images.

The simple single-impact model [36] was applied to fit the fluence-dependent amorphous sample fractions from XRD patterns (Fig. 4b), which has been independently confirmed by other techniques, such as Rutherford backscattering [29]. However, as noted in a previous study [30], a single-impact model may not be sufficient to accurately describe the formation of such complex track morphologies over a range of pyrochlore compositions. This may particularly apply to Zr-rich compositions, which have a noticeable defect-fluorite structured track shell (Fig. 2). A new phenomenological model has been proposed by Sattonnay et al. to better

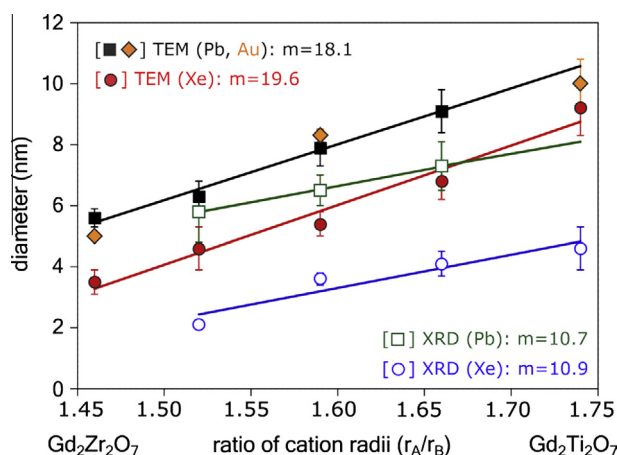


**Fig. 6.** Track diameters as directly measured from TEM images (Fig. 3) and indirectly deduced from peak fitting of XRD patterns (Fig. 4) for Xe (circles), Au (diamonds) and Pb (squares) ions. Straight lines are linear fits to the TEM (filled symbols) and XRD (open symbols) data. The overall track diameters are larger for TEM measurements for a given energy loss, and the rate of increase ( $m$  = slope) is consistent among each analytical technique.



account for the formation of heterogeneous tracks [30]. The single-impact mechanism of direct amorphization was extended with a single-overlap process that describes the formation of additional amorphous material by overlapping fluorite shells. However, this model does not account for a fluorite-creation mechanism related to post track-formation process, such as recovery and relaxation [1]. Independent of the applied track-formation model used for describing the ingrowth of the amorphous phase upon increasing irradiation fluence, the treatment of XRD patterns and, in particular, the determination of the amorphous sample fraction is not straightforward. Irradiation-induced amorphization can be quantitatively investigated by changes in the integrated peak intensities of either growing amorphous diffraction maxima [24] or by a reduction in intensity of maxima from crystalline domains [30]. A recent ion-beam investigation on  $\text{CaZrO}_3$  perovskite showed that the associated cross-sections for both procedures can differ, even for the same experimental data set [35]. At any rate, due to the complex and unknown relationship between integrated XRD-peak intensities and crystalline/amorphous phase distribution, neither method is an absolute measurement of the actual volume of material amorphized by swift heavy ions [40]. Additional contributions, such as defect-fluorite structure, defects and related strain effects will impact the behavior of XRD maxima upon irradiation. These contributions may show enhanced effects in the XRD patterns of pyrochlore compositions with a relatively limited amount of amorphization; this may explain the smaller slope for XRD diameters as compared with the results for TEM (Fig. 6). Without a detailed consideration of all contributing factors, the crystalline-to-amorphous transformation cannot be fully described by a simple analysis of increasing and decreasing integrated peak intensities. Related cross-section and diameter data may not represent the same track region in different pyrochlore compositions and, therefore, cannot be directly linked to a characteristic size of the complex ion tracks. The use of TEM bright-field images allow for the direct measure of the diameter of tracks based on visually estimating the position of the parallel boundaries between the modified contrast and the unchanged matrix. Since contrast variations are visible over the entire compositional range, induced in  $\text{Gd}_2\text{Zr}_2\text{O}_7$  by the defect-fluorite structure and in  $\text{Gd}_2\text{Ti}_2\text{O}_7$  mainly by the amorphous phase, both material modifications must contribute to the observed track contrast in bright-field images [24]. However, the overall track contrast is significantly weaker for Zr-rich compositions (Fig. 2d–f) [24]. At present, the effects of local strain fields to the modified contrast and its dependence on the pyrochlore composition are not fully understood. In particular for Ti-rich compositions, high-resolution TEM images evidence a pronounced strain halo surrounding the ion track (Fig. 2), which is possibly caused by a lattice misfit of amorphous-fluorite-pyrochlore phases at track core and shell boundaries, respectively (in direction from core to unirradiated matrix). Additional contributions may be due to a defect-enriched pyrochlore track halo. Taking into account the different sources of contrast, track diameters measured by means of TEM bright-field images may contain systematic errors beyond the statistical error. This may explain the larger slope of track diameters with  $r_A/r_B$  as compared with XRD diameters (Fig. 6).

Finally, Raman measurements are least suitable in quantitatively describing track formation in pyrochlore oxides. In this class of materials, Raman spectra consist of broad and overlapping vibrational modes with composition-dependent intensity ratios (Fig. 5a). Additionally, an irradiation-induced pronounced asymmetric background (Fig. 5b) obfuscates a reliable peak deconvolution and fitting. The exponential decrease of integrated Raman-peak intensities as a function of fluence depends critically on the selected vibrational mode. This yields somewhat different cross-section data for different vibration modes [27], with an unknown dependence on the amorphization process due to additional contributions from

disordering, strain, and defect formation. The Raman band at  $\sim 750\text{ cm}^{-1}$  associated with the amorphization process and its dependence on the actual amorphous sample fraction is not fully understood. Additional vibrational contributions from the amorphous phase may be contained in the large asymmetric background, in particular in the peak-like feature within the spectral region of the O–Gd–O bending mode (Fig. 5b). Noticeably, the  $\sim 750\text{ cm}^{-1}$  mode is already present in some pyrochlore compositions prior to irradiation (e.g.,  $\text{Gd}_2\text{ZrTiO}_7$ , Fig. 5a), and thus may not be exclusively related to the amorphous phase.

In conclusion, bright-field TEM, XRD, and Raman spectroscopy are limited to describe quantitatively the complex nanoscale damage structure of ion tracks in  $\text{Gd}_2\text{Zr}_{2-x}\text{Ti}_x\text{O}_7$  pyrochlore compositions. While all three techniques consistently indicate a decreasing irradiation resistance with  $r_A/r_B$ , direct atomic-scale characterization by means of high-resolution TEM is indispensable in order to fully explain the influence of chemical composition on the size and damage morphology. As displayed in Fig. 2, the overall track diameter increases from  $\text{Gd}_2\text{Zr}_2\text{O}_7$  to  $\text{Gd}_2\text{Ti}_2\text{O}_7$ . This has been previously explained within the framework of the analytical thermal spike model [41] as being the result of a gradual decrease in melting temperature with increasing Ti-content [24,30]. But other mechanisms, such as a suppressed recrystallization at the molten track boundary into the original pyrochlore structure in  $\text{Gd}_2\text{Ti}_2\text{O}_7$ , may contribute to the larger diameter. The damage morphology changes significantly with the pyrochlore composition (Fig. 2). MD simulations revealed that the track structure depends on complex competition among melting, disordering, and crystallization processes [1,2]. Thermodynamic and kinetic limitations of epitaxial crystallization in  $\text{Gd}_2\text{Ti}_2\text{O}_7$  and the stable formation of disorder due to similar cation radii in  $\text{Gd}_2\text{Zr}_2\text{O}_7$  may account for the dominating amorphous phase and defect-fluorite structure, respectively. High-resolution TEM images have been used to study in detail the internal structure of individual tracks as a function of  $dE/dx$  using several different ions. Since damage boundaries are less distinct for Zr-rich pyrochlore compositions, only  $\text{Gd}_2\text{Ti}_2\text{O}_7$  with its pronounced core-shell track structure has been investigated in detail.

### 3.2. Ion-track morphology in $\text{Gd}_2\text{Ti}_2\text{O}_7$ pyrochlore and its dependence on $dE/dx$

#### 3.2.1. High-resolution transmission electron microscopy

High-resolution TEM images display a strong influence of the energy loss on the size and internal structure of individual tracks in  $\text{Gd}_2\text{Ti}_2\text{O}_7$  after irradiation with  $^{101}\text{Ru}$ ,  $^{129}\text{Xe}$ ,  $^{181}\text{Ta}$ , and  $^{197}\text{Au}$  ions (Fig. 7a). The overall track size, i.e., amorphous core and defect-fluorite shell (Table 1), increases noticeably over the investigated energy-loss regime from  $\sim 5\text{ nm}$  for  $^{101}\text{Ru}$  ions ( $21.7\text{ keV/nm}$ ) to  $\sim 11\text{ nm}$  for  $^{197}\text{Au}$  ions ( $40.1\text{ keV/nm}$ ). In addition to the diameter increase, the internal track structure changes significantly over the range of ions studied: a core-shell structure changing from a defect-fluorite dominated shell at low  $dE/dx$  to predominantly amorphous tracks at high  $dE/dx$ . The amorphous fraction,  $f$ , was estimated for different ion tracks by the relative area ratio of amorphous core and defect-fluorite shell,  $r_a^2/r_{df+a}^2$  (Fig. 7b). From  $^{101}\text{Ru}$  ions to  $^{197}\text{Au}$  ions, the amorphous fraction increases from 11 to 67% following an exponential growth with  $dE/dx$ , while the respective track diameter increases by about a factor of two (Fig. 7c). It is interesting to note that the thickness of this fluorite shell remains, within about 1–2 nm, almost unchanged over the entire  $dE/dx$  regime. The presence of a fluorite phase for the titanate endmember,  $\text{Gd}_2\text{Ti}_2\text{O}_7$ , was questioned in a recent ion-beam study [30]. However, the current data, in particular for low  $dE/dx$ , indicate the existence of a defect-fluorite shell in the gadolinium titanate endmember (Fig. 7a). The lattice contrast with respect to the surrounding pyrochlore phase is different in the shell, and Fast Fourier

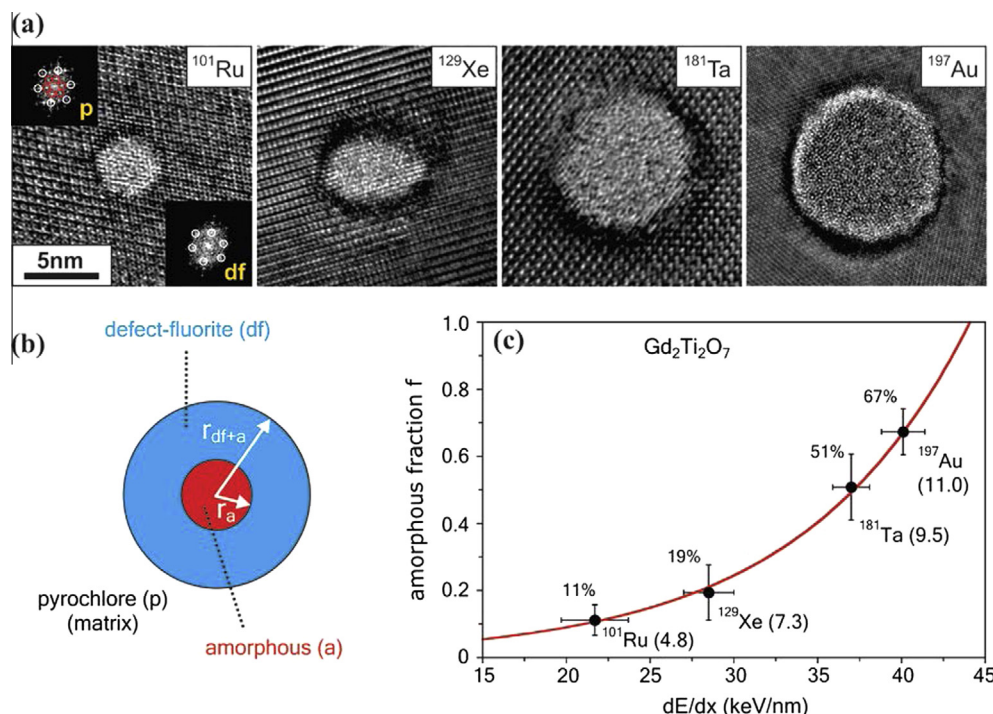


**Fig. 7.** (a) High-resolution TEM images of individual tracks in  $\text{Gd}_2\text{Ti}_2\text{O}_7$  pyrochlore produced by 1.1 GeV Ru ions (21.7 keV/nm), 1.4 GeV Xe ions (28.5 keV/nm), 2.0 GeV Ta ions (37.0 keV/nm), and 2.2 GeV Au ions (40.1 keV/nm). The track diameters increase systematically with  $dE/dx$  as shown from left to right. (b) Schematic of track morphology showing the amorphous core (red) surrounded by a defect-fluorite structured shell (blue) embedded in the pyrochlore matrix. Fast Fourier transform (FFT) analysis of TEM images confirm the crystalline phase of matrix (pyrochlore, p) and track shells (defect-fluorite, df), displayed in (a) for the Ru ion track. The loss of the spots in the inner circles corresponds to the loss of the long-range ordered pyrochlore superstructure leading to the defect-fluorite structure. (c) The amorphous fraction within an ion track (normalized core-to-shell ratio) increases significantly as a function of  $dE/dx$ . The error bars represent the  $dE/dx$  variation over the entire sample thickness (see Fig. 1 and Table 1) and the uncertainties of determining the area of amorphous core and entire track, respectively. The values in % represent the amorphous fraction, and the numbers in parenthesis are the total track diameters in nm (core + shell). The scale bar applies to all TEM images. (For interpretation of the references to color in this figure legend, the reader is referred to the web version of this article.)

Transform (FFT) analysis of high-resolution TEM images supported for all ion tracks that the shell in  $\text{Gd}_2\text{Ti}_2\text{O}_7$  consists primarily of the disordered, defect-fluorite structure. The FFT analysis is shown as two insets for the Ru track: one from the matrix and one from the track shell. As indicated by the circles, the matrix contains spots characteristic for the long-range ordered pyrochlore superstructure, while these diffraction spots are lost in the track shell and only the spots corresponding to the fluorite periodicity remain. This is indicative of the existence of a defect-fluorite structure in the track shell of the  $\text{Gd}_2\text{Ti}_2\text{O}_7$  endmember pyrochlore, which has been indirectly derived from TEM and XRD data at higher fluences with proceeding track overlap. Refinement of XRD patterns showed a mixture of disordered, defect-fluorite and ordered pyrochlore to coexist with the amorphous phase, and TEM detected defect-fluorite structured nanocrystals embedded in the amorphous matrix [23].

TEM-bright field imaging evidenced discontinuous contrast variations in  $\text{Gd}_2\text{Ti}_2\text{O}_7$  pyrochlore after irradiation to  $2 \times 10^{11}$  Ni ions/cm<sup>2</sup> (Fig. 8a). Ni-ion tracks obviously consist of parallel but discontinuous structures of darker contrast separated by larger gaps with no contrast difference to the surrounding matrix, whereas, the contrast of Ru-ion tracks is continuous but shows some intensity and diameter variation along their length (Fig. 8b). Tracks induced by Au ions are cylinders of uniform contrast and constant diameter (Fig. 8c). The mean track diameter increases significantly with  $dE/dx$  (Table 1). Following the description of the  $dE/dx$ -dependent ion-track morphology in yttrium iron garnet ( $\text{Y}_3\text{Fe}_5\text{O}_{12}$ ) [39], Ni tracks are discontinuous, consisting of separate damage domains (Fig. 8a). The relative length of the individual domains along the ion trajectory is large as compared with the confining gaps, which suggests that the critical energy loss for track

formation  $(dE/dx)_c$  is close to but above the energy loss of Ni ions of 10.9 keV/nm. Tracks produced with Ru ions ( $dE/dx = 21.7$  keV/nm) are continuous but show strong diameter variations along their lengths (Fig. 8b) as a result of an energy loss close to the track formation threshold [39,42]. For ion beams of  $\sim 11$  MeV/u specific energy, continuous tracks will form in  $\text{Gd}_2\text{Ti}_2\text{O}_7$  if the energy loss exceeds  $(dE/dx)_c \sim 11$  keV/nm, which is in good agreement with experimental data by Moll et al. (11–13 keV/nm) using heavy ions of slightly smaller specific energy (4.5–9.3 MeV/u) [28]. Based on the evolution of track radii with the square root of  $dE/dx$ , a critical threshold of about 11.5–13 keV/nm was established, below which swift heavy ions can no longer directly induce amorphization within single tracks in  $\text{Gd}_2\text{Ti}_2\text{O}_7$  [28]. While the internal structure of Ru and Au ion tracks is clearly revealed by high-resolution TEM images in plan view (Fig. 7a), overlapping damaged and undamaged layers makes imaging of Ni tracks rather difficult. Fast Fourier Transform (FFT) analysis of high-resolution TEM images in plan view indicates that the isolated damage domains in  $\text{Gd}_2\text{Ti}_2\text{O}_7$  irradiated with  $2 \times 10^{11}$  Ni ions/cm<sup>2</sup> contain disordered, defect-fluorite (df) structure (Fig. 9a); no amorphization was indicated in the TEM analysis for this ion fluence, and the surrounding matrix was confirmed as being the pyrochlore (p) starting structure. No crystalline-to-amorphous phase transformation was evident in the corresponding XRD pattern (Fig. 9d) and refinement yield only the ordered pyrochlore phase without any indication of disordering. The well-separated damage domains are probably too small to show up in the XRD pattern. They start to overlap at higher fluences ( $5 \times 10^{12}$  ions/cm<sup>2</sup>), and the accumulation of multiple tracks results in the formation of heavily damaged zones (Fig. 9b) that lead eventually to complete amorphization after irradiation with



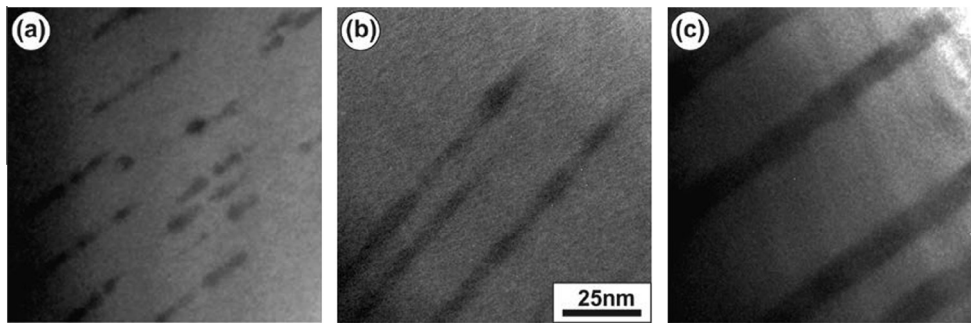


**Fig. 8.** Bright-field TEM images of non-overlapping tracks in  $\text{Gd}_2\text{Ti}_2\text{O}_7$  pyrochlore produced by (a) 0.6-GeV Ni ions (10.9 keV/nm), (b) 1.1-GeV Ru ions (21.7 keV/nm), and (c) 2.2-GeV Au ions (40.1 keV/nm). Tracks are discontinuous for Ni ions, continuous and inhomogeneous for Ru ions, and continuous and homogeneous for Au ions. The track diameter increases as function of  $dE/dx$ . The scale bar applies to all TEM images.

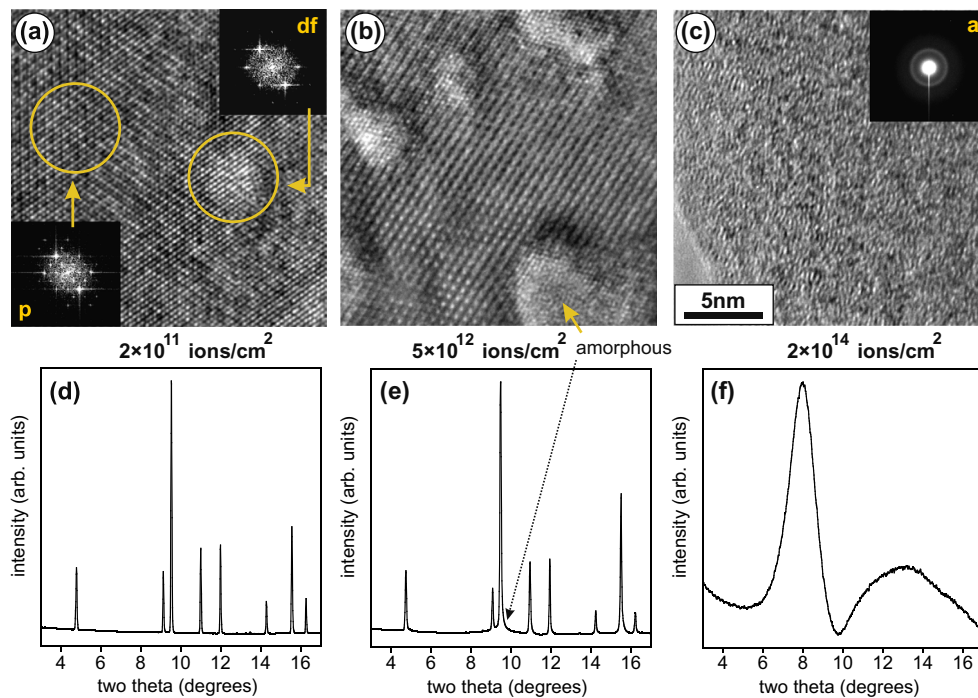


**Fig. 9.** High-resolution TEM images of  $\text{Gd}_2\text{Ti}_2\text{O}_7$  pyrochlore in plan view and corresponding XRD patterns after irradiation with 0.6-GeV Ni ions (10.9 keV/nm) at a fluence of (a and d)  $2 \times 10^{11} \text{ cm}^{-2}$ , (e)  $5 \times 10^{12} \text{ cm}^{-2}$ , and (f)  $2 \times 10^{14} \text{ cm}^{-2}$ . Fast Fourier transform (FFT) analysis of TEM images indicate that (a) well separated damage regions are defect-fluorite, *df*, domains embedded in the pyrochlore, *p*, matrix; (b) localized amorphization occurs in connected damage regions, and (c) the sample is fully amorphous, *a*, after multiple track overlaps for the highest fluence. XRD patterns confirm the TEM findings of (e) partial and (f) full amorphization. Disorder of about 5% to the defect-fluorite phase was evident in the sample irradiated to  $5 \times 10^{12} \text{ cm}^{-2}$ . The scale bar applies to all TEM images.

$2 \times 10^{14} \text{ Ni ions/cm}^2$  (Fig. 9c). The corresponding XRD pattern at  $5 \times 10^{12} \text{ ions/cm}^2$  confirms the finding by TEM and shows minor indication of the onset of amorphization by the weak background increase at the most intense diffraction maximum (see arrow in Fig. 9e). Refinement of the pattern show also evidence of additional disorder with approximately 5% of defect-fluorite coexisting with pyrochlore phase and the small amorphous domains. The XRD pattern of the sample irradiated to the maximum fluence confirms that  $2 \times 10^{14} \text{ Ni ions/cm}^2$  lead to a fully amorphous sample (Fig. 9f). The existence of fluorite-structured nano-domains at smaller fluences along Ni ion tracks can be understood by extrapolating the track structure of Ru ions (Fig. 7a) to smaller  $dE/dx$ . An amorphous track region can no longer be directly induced if the diameter falls below a critical size limit – on the order of the fluorite-shell thickness in Fig. 7a. An alternative explanation for the lack of amorphization is a complete damage recovery and crystallization after track formation. Isolated defect-fluorite layers embedded in a pyrochlore matrix have been also reported in  $\text{Gd}_2\text{Ti}_2\text{O}_7$  pyrochlore after irradi-

ation with high-dose, low-energy ions in the nuclear  $dE/dx$  regime [43]. The onset of amorphization at higher Ni fluences ( $5 \times 10^{12} \text{ ions/cm}^2$ ) is related to the beginning of overlapping damage domains (Fig. 9b). The amorphous phase may form by a second ion impact within a defect-fluorite area induced by a preceding ion [30]. However, if the formation of the defect-fluorite structure within tracks is the result of a complete damage recovery and crystallization as indicated by previous molecular dynamics simulations [1,2], a second ion impact within a defect-fluorite region may result again in the defect-fluorite phase if the thermal conductivity remains similar in the previously modified region. Thus, the existence of amorphous domains at higher fluences of Ni irradiation may be due to increasing size of defect-fluorite volumes within  $\text{Gd}_2\text{Ti}_2\text{O}_7$  and size-dependent thermodynamic constraints related with the formation of this nonequilibrium phase [1]. It has been previously shown that nanoscale manipulation by energetic projectiles and in particular, the formation of radiation-induced nanocrystals, can lead to modifications of thermodynamic path-

ways in  $\text{Gd}_2\text{Zr}_2\text{O}_7$  pyrochlore [44]. A high-pressure phase, thermodynamically unstable in bulk form at ambient pressure, was quenched after swift heavy ion irradiation. Based on quantum mechanical calculations, the appearance of this phase was attributed to the effect of surface energy, which makes it stable below a threshold grain size [44]. This has been also observed for other materials [45,46]. The heterogeneous strain field formed around amorphous ion tracks (see Fig. 7a) may also affect the stability of the non-equilibrium defect fluorite phase in this material. With increasing irradiation fluence, the overlap of individual fluorite domains may surpass a critical size limit for their metastable existence leading to amorphization via spontaneous transformations (Fig. 9b) which results to complete amorphization at extremely high fluences in the multi-track overlap regime (Fig. 9c and f).

In summary, high-resolution TEM images of tracks in  $\text{Gd}_2\text{Ti}_2\text{O}_7$  induced by different ions confirm the clear increase of the track diameter with  $dE/dx$  as indicated by other characterization techniques. The track morphology changes significantly over the studied energy-loss regime with predominantly defect-fluorite structured tracks at low  $dE/dx$  and amorphous tracks at high  $dE/dx$ . Continuous tracks form if the ion energy loss exceeds a critical value of  $(dE/dx)_c \sim 11$  keV/nm. Due to the weak contrast (Fig. 2), high-resolution TEM could not be completed in other pyrochlore compositions for different ion irradiations. However, conclusions concerning how track size and damage morphology change with  $dE/dx$  over the  $\text{Gd}_2\text{Zr}_{2-x}\text{Ti}_x\text{O}_7$  binary system can be obtained indirectly by combining results from (i) qualitative characterization of different compositions with bright-field TEM, XRD, and Raman, and (ii) quantitative analysis of gadolinium titanate pyrochlore by high-resolution TEM: The significant increase of amorphization with  $dE/dx$ , is possibly the result of a growing amorphous track core in all Ti-containing pyrochlore compositions consistent with the results for  $\text{Gd}_2\text{Ti}_2\text{O}_7$  (Fig. 7). The thickness of the fluorite-shell is probably constant in other pyrochlore compositions over a range of  $dE/dx$  with a core-shell ratio determined by the ratio  $r_A/r_B$  (larger shells for increasing Zr-content). For the Zr-endmember,  $\text{Gd}_2\text{Zr}_2\text{O}_7$ , amorphization can no longer be induced by swift heavy ions even for maximum values of  $dE/dx$ .

### 3.2.2. Model description

The existence of defect-fluorite structured track regions in  $\text{Gd}_2\text{Zr}_{2-x}\text{Ti}_x\text{O}_7$  pyrochlore was explained by previous molecular dynamics (MD) calculations [1,2] as being the result of damage recovery and epitaxial crystallization at the interface of a molten track and the surrounding pyrochlore matrix. The crystallization was shown to advance from the outer (cooler) boundary of the molten area towards the inner (hotter) central region at the late stage of the track-formation process [1,2]. Determined by the quench rate of the specific pyrochlore composition, the formation of the disordered fluorite phase may not be complete, leading to a complex core-shell track morphology (Fig. 7a). If the crystallization front proceeds at a constant velocity for different ion species, a similar fluorite-shell thickness can be expected over a range of  $dE/dx$  values. This is consistent with the experimental observation from high-resolution TEM showing a 1–2 nm defect-fluorite shell in  $\text{Gd}_2\text{Ti}_2\text{O}_7$  from Ru to Au ions (Fig. 7a). In addition to the kinetic limitations of the quenching process, the relatively small fluorite shell in gadolinium titanate pyrochlore may be the result of thermodynamic constraints. The large difference in the ionic radii of Gd and Ti prevent disordering over the cation sites through antisite defect formation, making the defect-fluorite structure energetically unfavorable. Within the nanoscale environment of swift heavy ion tracks however, this nonequilibrium phase may exist metastably as a thin shell surrounding the amorphous core [3]. If a critical fluorite-shell size of about 1–2 nm is reached during the quenching process, the formation of the amorphous phase may be the only

possible structural outcome (resulting in the remaining amorphous core). This concept agrees well with the high-resolution TEM characterization of small damage domains produced by Ni ions (Fig. 9). While well isolated domains of about 2 nm consist of the defect-fluorite structure (Fig. 9a), overlapping domains contain a growing fraction of amorphous material (Fig. 9b). A quantitative description of the track morphology, in particular, the relative size of fluorite shell vs. amorphous core for different  $dE/dx$ , is at present not feasible and requires additional MD calculations.

Different theoretical models have been proposed since the beginning of 1950s to explain and describe the occurrence of tracks after irradiation with swift heavy ions slowing down in matter through ionizations and electronic excitations (electronic  $dE/dx$ ). There exists no conclusive description that accounts for all aspects of the track-formation process, and the origin of many irradiation effects remains controversial. Models that have been most frequently cited over the past decades are the ionic-spike model for insulators by Fleischer et al. [47] and the thermal-spike model [48] initially proposed by Seitz and Koehler [49]. The ionic-spike model assumes that energetic ions create cylindrical regions of highly ionized matter along their trajectories. Large repulsive electrostatic forces build-up within tracks prior to restoration of electric charge neutrality, giving rise to a violent Coulomb explosion within  $10^{-15}$  to  $10^{-13}$  s. This phenomenon leads to bond breaking and atomic disorder within a local region of the atomic-scale structure. The model was developed based on the initial experimental observation that only insulators are able to record ion tracks. With the advent of large ion-beam facilities, numerous experiments have shown, however, that high energy ions with an energy loss in the electronic regime are also efficient in creating radiation damage in semi-conductor materials [50–52] and selected metals [53,54], including in particular amorphous metallic alloys [55,56]. The inelastic thermal spike model has recently received renewed attention. A number of ion-track phenomenon can be explained with this model for metals [57], semiconductors [58,59], and insulators [5,60], including an explanation of the so-called velocity effect [4,5]. Also sputtering rates by high-energy ion beams have been successfully modeled for metallic [61] and insulating [62] targets.

### 4. Calculations with the inelastic thermal spike model (i-TS)

Within the thermal-spike model, the dissipation of the ion energy deposited to the target is considered in two steps. (i) Initially the ions transfer their energy to the electrons of the target. By electron–electron interactions, this energy is shared among other electrons and finally transferred to the lattice by electron–phonon coupling. (ii) The transferred energy is dissipated among the atoms and induces a high-temperature spike along the incident ion path. The spike temperature may exceed the energy to induce a solid–liquid transformation, and in some cases even a liquid–vapor phase change [63]. Track formation is assumed to be the result of a rapid quenching of the cylinder of highly excited and molten matter. Due to the small volume of the thermal-spike zone (several nm in diameter), extremely high cooling rates of up to  $\sim 10^{15}$  K s<sup>−1</sup> may be reached producing an equilibrated track region in the solid state within  $\sim 10^{-11}$  s. Bringa et al. [64] showed by means of MD calculations that atomic displacements due to a possible ionic spike are thermalized within a time of  $\sim 2 \times 10^{-13}$  s, i.e., prior to the thermal spike ( $\sim 10^{-12}$  s) and thus may be annealed by the subsequent temperature rise.

Over the last years, the inelastic thermal-spike model was refined in several steps [5,65], and the following description will be restricted to its application to insulators [60]. The calculations are based on two coupled equations governing the energy diffusion on the electron and lattice subsystem in cylindrical geometry [66]. A complete numerical solution of the two equations has been

developed in order to introduce directly the energy distribution to the electronic subsystem as proposed by Zhang et al. [67] taking into account materials properties, as well as beam energy [5]. The energy distribution in the electronic subsystem has been validated by Monte Carlo calculations [68,69]. The main parameters in the model are the energy necessary to reach the solid–liquid phase change and the electron–phonon coupling parameter represented by the mean free electron–phonon path ( $\lambda$ ). For a number of insulators, in which ions are assumed to produce tracks via quenching of a molten phase,  $\lambda$  scales with the optical band gap energy [4,60]. Typical thermal-spike simulations consist of solving the two thermal-transport equations by using  $\lambda$  as a free parameter to fit experimental track-diameter data. At present, this approach cannot be applied to ion tracks in  $\text{Gd}_2\text{Ti}_2\text{O}_7$ . While the melting temperature is approximately 2093 K [70], no information is available on the thermal energy necessary to produce a molten phase in this material.

Thermal-spike simulations for  $\text{Gd}_2\text{Ti}_2\text{O}_7$  were based on a different strategy with the aim to determine a critical energy density ( $E_t$ ) required for track formation, which is associated with inducing a melt in the material. This energy density was treated as a free parameter, while  $\lambda$  was used as a fixed value deduced from optical band gap calculations [71]. According to the previously indicated scaling procedure [70], the band gap in  $\text{Gd}_2\text{Ti}_2\text{O}_7$  is 3.3 eV, which corresponds to  $\lambda = 4.9$  nm [71]. The energy density,  $E_t$ , is adjusted by means of fit routines such that the i-TS simulations reproduce the experimentally determined track diameters. The total track diameter from high-resolution TEM images was used, which includes both amorphous core and defect-fluorite shell, ( $2 \cdot r_{df+a}$  in Fig. 7b). As mentioned above, diameters from high-resolution TEM represent the most reliable experimental data set (Table 1). In contrast to previous i-TS simulations, which focused only on amorphous tracks, the fluorite-structured shell was included in the present approach since MD simulations [1,2] suggest that this region was part of the initially molten track zone. All calculations were performed for ions with a specific energy of 7 MeV/u. This value represents the mean energy for all ion irradiations, taking into account a sample thickness of 40  $\mu\text{m}$  and corresponding energy reduction from 11.1 MeV/u (sample surface) to  $\sim 2.0$  MeV/u (sample back side). All samples were crushed into a powder after irradiation for TEM characterization and the experimental data (Fig. 7a) cover this energy range independent of the almost constant  $dE/dx$  (Fig. 1). Fig. 10 a and b present i-TS calculations for Ru and Au ions

displaying the deposited energy density to the lattice in eV per atom as a function of (i) time after the ion impact and (ii) cylinder diameter with respect to the original ion trajectory. The solid horizontal lines correspond to the high-resolution TEM track diameters for Ru (4.8 nm) and Au (11.0 nm) ions, respectively. The energy densities to produce a molten track of given size is  $E_t = 0.94$  eV/at for Ru ions and  $E_t = 0.8$  eV/at for Au ions. The same procedure was applied to Xe and Ta ions (Fig. 7a) yielding an average  $\langle E_t \rangle = 0.9 \pm 0.1$  eV/at for all ion species. This value is considered as the mean energy density required for the formation of swift heavy ion tracks in  $\text{Gd}_2\text{Ti}_2\text{O}_7$ . The evolution of the calculated track diameters as function of  $dE/dx$  based on  $\langle E_t \rangle = 0.9$  eV/at is displayed in Fig. 11a (solid curve) demonstrating the good agreement with experimental results (round, red data points). The average energy density of 0.9 eV/at agrees also with results from previous i-TS calculations for track formation in the same pyrochlore by U ions of specific energy below 0.5 MeV/u ( $\langle E_t \rangle = 0.8$  eV/at) [32,72].

In addition to the calculations described above, the same approach was applied for an energy density  $E_t = 0.6$  eV/at (Fig. 11a, dashed line). This value is based on the thermal energy required to reach the melting temperature of 2093 K in  $\text{Gd}_2\text{Ti}_2\text{O}_7$  from 300 K, resulting from a specific heat of 0.53 J/g/K (according to the Dulong–Petit law). Thermal-spike calculations with this energy density as function of  $dE/dx$  (dashed curve in Fig. 11a) reveal that 0.6 eV/at cannot reproduce the experimental track diameters. The higher energy density of  $E_t = 0.9$  eV/at (or 950 kJ/mol) can be understood in terms of latent heat. The difference between 0.6 and 0.9 eV/at corresponds to a latent heat of 360 kJ/mol, which is in good agreement with  $\sim 350$  kJ/mol, the latent heat determined experimentally for  $\text{La}_2\text{Zr}_2\text{O}_7$  pyrochlore [73]. Thus, the energy density  $E_t = 0.9$  eV/at can be defined as the energy to melt the material, which leads by rapid quenching to the formation of small, predominantly fluorite-structured tracks and large amorphous tracks with a fluorite shell at low and high  $dE/dx$ , respectively.

Thermal-spike calculations are helpful in predicting the  $(dE/dx)_c$  threshold for track formation (Fig. 11b). The solid sloped line is the energy density,  $E_{\text{max}}$ , at the ion trajectory (cylinder size = 0 nm) induced from the maximum deposited energy. Similar as for  $E_t$ , this value can be inferred from Fig. 10 for Ru (1.7 eV/at) and Au ions (3.2 eV/at). Plotting  $E_t$ , the energy needed for melting, as a function of  $dE/dx$  (solid horizontal line in Fig. 11b) and extrapolating to the sloped  $E_{\text{max}}$  line provides with a  $(dE/dx)_c$  threshold of 11.7 keV/nm, which is in agreement with the predicted value based on the

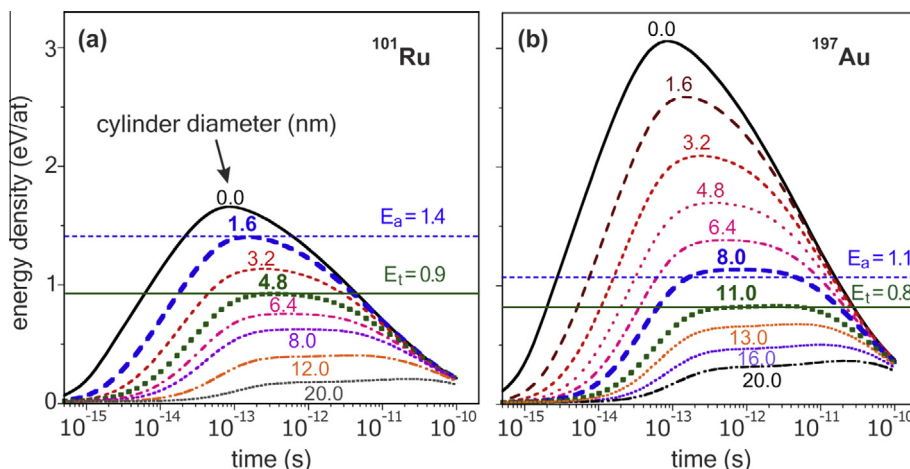


**Fig. 10.** Inelastic thermal spike calculations of the evolution of the energy density deposited to the target atoms in  $\text{Gd}_2\text{Ti}_2\text{O}_7$  versus time for different diameters of the track cylinder (given in nm): (a) Ru ions and (b) Au ions of 7 MeV/u. Horizontal lines indicate the required energy density to obtain track diameters in agreement with experimental data from high-resolution TEM (Table 1). The solid and dashed lines are the critical energy densities in eV/at corresponding to core-shell tracks,  $E_t$ , and amorphous track cores,  $E_a$ , respectively.



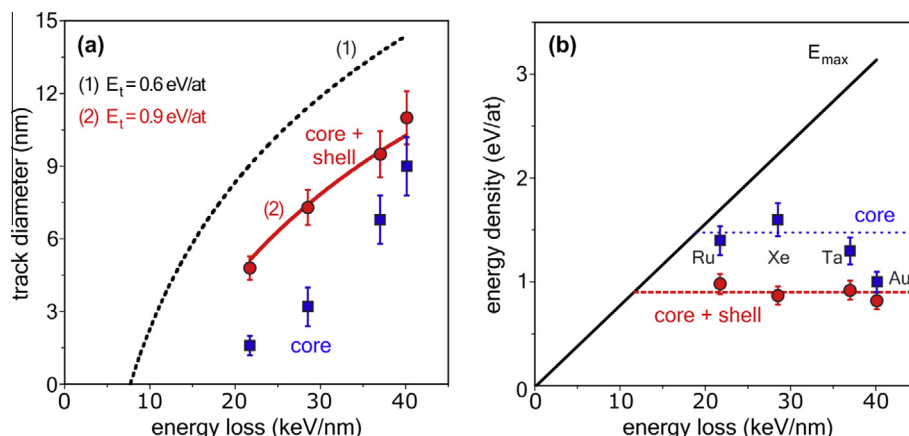


**Fig. 11.** (a) Experimental track diameters for different ion beams in  $Gd_2Ti_2O_7$  from high-resolution TEM measurements as a function of  $dE/dx$ : core-shell tracks (red circles) and amorphous track cores (blue squares). The solid red and dashed black curves are the results of thermal-spike calculations based on  $E_t = 0.90$  eV/at and  $E_t = 0.56$  eV/at, respectively. (b) Data points are fit values for the critical energy density  $E_t$  (red circle) and  $E_a$  (blue squares) required to reproduce the experimental track diameters induced by  $^{101}Ru$ ,  $^{129}Xe$ ,  $^{181}Ta$ , and  $^{197}Au$  ions. The solid sloped line represents the maximum energy  $E_{max}$  deposited to the target atoms according to the inelastic thermal spike approach. Intersections of  $E_t$  (solid horizontal line) and  $E_a$  (dashed horizontal line) with  $E_{max}$  provides an estimate of the  $(dE/dx)_c$  thresholds for the formation of core-shell tracks and amorphous cores, respectively.

experimental results in this study ( $\sim 11$  keV/nm) and a previous investigation [28].

Finally, despite the agreement among MD calculations [1,2], alternative formation mechanisms of the core-shell track structure in pyrochlore cannot be fully excluded. The fluorite shell may not be the result of damage recovery and crystallization from a melt, but rather formed directly together with the amorphous core. If the latter is considered as being formed by a molten track, a different energy density must be taken into account for i-TS simulations. This energy density,  $E_a$  ("a" denoting for the amorphous core), is deduced following the same approach as described above (dashed horizontal lines in Fig. 10). The experimental data represent the amorphous core diameters from high-resolution TEM measurements (Figs. 7a and 11a, Table 1). The resulting energy densities  $E_a$  for different ion-track cores are shown in Fig. 11b (blue squares). Compared with the corresponding  $E_t$  required to form core-shell tracks,  $E_a$  is systematically larger and varies over the investigated  $dE/dx$  regime between 1.5 and 1.0 eV/at. The formation of larger amorphous cores for ions with higher  $dE/dx$  (Ta and Au) requires a smaller energy density ( $E_a$  approaching  $E_t$ ). The intersection of the larger  $E_a$  for ions with smaller  $dE/dx$  (dashed horizontal line in Fig. 11b) with  $E_{max}$  (sloped solid line in Fig. 11b) yields a critical energy loss of  $(dE/dx)_a \sim 19$  keV/nm for the formation of an amorphous core within swift heavy ion tracks. This threshold  $(dE/dx)_a$  is in agreement with the absence of amorphization in individual (non-overlapping) Ni ion tracks (damage domains).

## 5. Conclusions

Polycrystalline samples of  $Gd_2Zr_{2-x}Ti_xO_7$  pyrochlore ( $x = 0, 0.5, 1, 1.5$ , and 2) were irradiated with  $^{58}Ni$ ,  $^{101}Ru$ ,  $^{129}Xe$ ,  $^{181}Ta$ ,  $^{197}Au$ ,  $^{208}Pb$ , and  $^{238}U$  ions at an energy of 11.1 MeV/u (atomic mass unit u). Complementary characterization with bright-field TEM, synchrotron XRD, and Raman spectroscopy showed a consistent trend of ion-induced structural modifications: (i) for a given pyrochlore composition, a significant increase of amorphization with the electronic energy loss,  $dE/dx$ ; (ii) for a given  $dE/dx$ , an increase of amorphization with the Ti-content of the pyrochlore. A quantitative analysis based on direct bright-field TEM images and indirect cross-section data from Raman spectroscopy or XRD measurements is, for the complex track-structure in pyrochlore, problematic due to length-scale limitations of each technique. The size

and damage morphology of individual tracks in  $Gd_2Ti_2O_7$  induced by  $^{58}Ni$ ,  $^{101}Ru$ ,  $^{129}Xe$ ,  $^{181}Ta$ , and  $^{197}Au$  ions was additionally analyzed by means of high-resolution TEM. The track morphology changes significantly as a function of energy-loss, with predominantly defect-fluorite structured tracks at low  $dE/dx$  and amorphous tracks at high  $dE/dx$ . Continuous tracks form if the ion energy loss exceeds a critical value of  $(dE/dx)_c \sim 11$  keV/nm. The significantly increasing amorphous core accounts for the size increase of tracks as function of  $dE/dx$ , while the thickness of the defect-fluorite structured outer shell remains almost constant. Inelastic thermal-spike calculations were used to deduce critical energy densities for the complex core-shell morphologies of tracks in  $Gd_2Ti_2O_7$ , induced by ions of different  $dE/dx$ .

## Acknowledgement

This work was supported as part of the Materials Science of Actinides, an Energy Frontier Research Center funded by the U.S. Department of Energy, Office of Science, Office of Basic Energy Sciences under Award Number DE-SC0001089 (UM, UT) and Contract DE-AC05-00OR22725 (ORNL). The use of CHES beam is supported by the NSF & NIH/NIGMS via NSF award DMR-0225180. One of the authors (M.T.) is grateful to Professor Ewing at the University of Michigan for the financial support for his two-month visit.

## References

- [1] J.M. Zhang, M. Lang, R.C. Ewing, R. Devanathan, W.J. Weber, M. Toulemonde, Nanoscale phase transitions under extreme conditions within an ion track, *J. Mater. Res.* 25 (2010) 1344–1351.
- [2] J.W. Zhang, M. Lang, R.C. Ewing, U. Becker, Multi-scale simulation of structural heterogeneity of swift-heavy ion tracks in complex oxides, *J. Phys. Condens. Matter* 25 (2012) 135001.
- [3] C.L. Tracy, M. Lang, J.M. Zhang, F.X. Zhang, Z.W. Wang, R.C. Ewing, Structural response of  $A_2TiO_5$  ( $A = La, Nd, Sm, Gd$ ) to swift heavy ion irradiation, *Acta Mater.* 60 (2012) 4477–4486.
- [4] A. Meftah, J.M. Costantini, N. Khalfaoui, S. Boudjadar, J.P. Stoquert, F. Studer, M. Toulemonde, Experimental determination of track cross-section in  $Gd_3Ga_5O_{12}$  and comparison to the inelastic thermal spike model applied to several materials, *Nucl. Instr. Meth. B* 237 (2005) 563–574.
- [5] M. Toulemonde, W. Assmann, C. Dufour, A. Meftah, F. Studer, C. Trautmann, Experimental phenomena and thermal spike model description of ion tracks in amorphisable inorganic insulators, *Mat. -Fys. Medd.* 52 (2006) 263–292.
- [6] S. Mookerjee, M. Beuve, S.A. Khan, M. Toulemonde, A. Roy, Sensitivity of ion-induced sputtering to the radial distribution of energy transfers: a molecular dynamics study, *Phys. Rev. B* 78 (2008) 045435.

- [7] R. Devanathan, W.J. Weber, J.D. Gale, Radiation tolerance of ceramics – insights from atomistic simulation of damage accumulation in pyrochlores, *Energy Environ. Sci.* 3 (2010) 1551–1559.
- [8] M. Huang, D. Schwen, R.S. Averback, Molecular dynamic simulation of fission fragment induced thermal spikes in  $\text{UO}_2$ : sputtering and bubble re-solution, *J. Nucl. Mater.* 399 (2010) 175–180.
- [9] D. Schwen, E.M. Bringa, Atomistic simulations of swift ion tracks in diamond and graphite, *Nucl. Instr. Meth. B* 256 (2007) 187–192.
- [10] M.A. Subramanian, G. Aravamudan, G.V. Subba Rao, Oxide pyrochlores – a review, *Prog. Solid State Chem.* 15 (1983) 55–143.
- [11] S.X. Wang, B.D. Begg, L.M. Wang, R.C. Ewing, W.J. Weber, K.V. Govidan Kutty, Radiation stability of gadolinium zirconate: a waste form for plutonium disposition, *J. Mater. Res.* 14 (1999) 4470–4473.
- [12] K.E. Sickafus, L. Minervini, R.W. Grimes, J.A. Valdez, M. Ishimaru, F. Li, K.J. McClellan, T. Hartmann, Radiation tolerance of complex oxides, *Science* 289 (2009) 748–751.
- [13] W.J. Weber, R.C. Ewing, Plutonium immobilization and radiation effects, *Science* 289 (2000) 2051–2052.
- [14] R.C. Ewing, W.J. Weber, J. Lian, Nuclear waste disposal—pyrochlore ( $\text{A}_2\text{B}_2\text{O}_7$ ): nuclear waste form for the immobilization of plutonium and “minor” actinides, *J. Appl. Phys.* 95 (2004) 5949–5971.
- [15] K.E. Sickafus, R.W. Grimes, J.A. Valdez, A. Cleave, M. Tang, M. Ishimaru, S.M. Corish, C.R. Stanek, B.P. Uberuaga, Radiation-induced amorphization resistance and radiation tolerance in structurally related oxides, *Nat. Mater.* 6 (2007) 217–223.
- [16] J. Lian, L.M. Wang, J. Chen, K. Sun, R.C. Ewing, J. Matt Farmer, L.A. Boatner, The order–disorder transition in ion-irradiated pyrochlore, *Acta Mater.* 51 (2003) 1493–1502.
- [17] J. Lian, X.T. Zu, K.V.G. Kutty, J. Chen, L.M. Wang, R.C. Ewing, Ion-irradiation-induced amorphization of  $\text{La}_2\text{Zr}_2\text{O}_7$  pyrochlore, *Phys. Rev. B* 66 (2002) 054108.
- [18] J. Lian, J. Chen, L.M. Wang, R.C. Ewing, J.M. Farmer, L.A. Boatner, K.B. Helean, Radiation-induced amorphization of rare-earth titanate pyrochlores, *Phys. Rev. B* 68 (2003) 134107.
- [19] W.J. Weber, R.C. Ewing, C.R.A. Catlow, T. Diaz de la Rubia, L.W. Hobbs, C. Kinoshita, H.J. Matzke, A.T. Motta, M. Nastasi, E.K.H. Salje, E.R. Vance, S.J. Zinkle, Radiation effects in crystalline ceramics for the immobilization of high-level nuclear waste and plutonium, *J. Mater. Res.* 13 (1998) 1434–1484.
- [20] S.X. Wang, L.M. Wang, R.C. Ewing, K.V.G. Kutty, Ion irradiation effects for two pyrochlore compositions:  $\text{Gd}_2\text{Ti}_2\text{O}_7$  and  $\text{Gd}_2\text{Zr}_2\text{O}_7$ , *Mater. Res. Soc. Symp. Proc.* 540 (1999) 355–360.
- [21] M.K. Patel, V. Vijayakumar, D.K. Avasthi, S. Kailas, J.C. Pivin, V. Grover, B.P. Mandal, A.K. Tyagi, Effect of swift heavy ion irradiation in pyrochlores, *Nucl. Instr. Meth. B* 266 (2008) 2898–2901.
- [22] G. Sattonnay, S. Moll, L. Thomé, C. Legros, M. Herbst-Ghysel, F. Garrido, J.M. Costantini, C. Trautmann, Heavy-ion irradiation of pyrochlore oxides: comparison between low and high energy regimes, *Nucl. Instr. Meth. B* 266 (2008) 3043–3047.
- [23] M. Lang, F.X. Zhang, J. Lian, C. Trautmann, Z.W. Wang, R.C. Ewing, Structural modifications of  $\text{Gd}_2\text{Zr}_{2-x}\text{Ti}_x\text{O}_7$  pyrochlore induced by swift heavy ions: disordering and amorphization, *J. Mater. Res.* 24 (2009) 1322–1334.
- [24] M. Lang, J. Lian, J.M. Zhang, F.X. Zhang, W.J. Weber, C. Trautmann, R. Neumann, R.C. Ewing, Single-ion tracks in  $\text{Gd}_2\text{Zr}_{2-x}\text{Ti}_x\text{O}_7$  pyrochlores irradiated with swift heavy ions, *Phys. Rev. B* 79 (2009) 224105.
- [25] J.M. Zhang, M. Lang, J. Lian, J. Liu, C. Trautmann, S. Della-Negra, M. Toulemonde, R.C. Ewing, Liquid-like phase formation in  $\text{Gd}_2\text{Zr}_2\text{O}_7$  by extremely ionizing irradiation, *J. Appl. Phys.* 105 (2009) 113510.
- [26] M. Lang, F.X. Zhang, J.M. Zhang, J.W. Wang, J. Lian, W.J. Weber, B. Schuster, C. Trautmann, R. Neumann, R.C. Ewing, Review of  $\text{A}_2\text{B}_2\text{O}_7$  pyrochlore response to irradiation and pressure, *Nucl. Instr. Meth. B* 268 (2010) 2951–2959.
- [27] G. Sattonnay, S. Moll, L. Thomé, C. Decorse, C. Legros, P. Simon, J. Jagielski, J. Jozwik, I. Monnet, Phase transformations induced by high electronic excitation in ion irradiated  $\text{Gd}_2(\text{Zr}_{1-x}\text{Ti}_x)_2\text{O}_7$  pyrochlores, *J. Appl. Phys.* 108 (2010) 103512.
- [28] S. Moll, G. Sattonnay, L. Thome, J. Jagielski, C. Legros, I. Monnet, Swift heavy ion irradiation of pyrochlore oxides: electronic energy loss threshold for latent track formation, *Nucl. Instr. Meth. B* 268 (2010) 2933–2936.
- [29] S. Moll, G. Sattonnay, L. Thome, J. Jagielski, C. Decorse, P. Simon, I. Monnet, W.J. Weber, Irradiation damage in  $\text{Gd}_2\text{Ti}_2\text{O}_7$  single crystals: ballistic versus ionization processes, *Phys. Rev. B* 84 (2011) 064115.
- [30] G. Sattonnay, C. Grygiel, I. Monnet, C. Legros, M. Herbst-Ghysel, L. Thomé, Phenomenological model for the formation of heterogeneous tracks in pyrochlores irradiated with swift heavy ions, *Acta Mater.* 60 (2012) 22–34.
- [31] G. Sattonnay, S. Moll, L. Thomé, C. Legros, A. Calvo, M. Herbst-Ghysel, C. Decorse, I. Monnet, Effect of composition on the behavior of pyrochlores irradiated with swift heavy ions, *Nucl. Instr. Meth. B* 272 (2012) 261–265.
- [32] I. Jozwik-Biala, J. Jagielski, L. Thomé, B. Arey, L. Kovarik, G. Sattonnay, A. Debelle, I. Monnet, HRTEM study of track evolution in 120-MeV U irradiated  $\text{Gd}_2\text{Ti}_2\text{O}_7$ , *Nucl. Instr. Meth. B* 286 (2012) 258–261.
- [33] J.F. Ziegler, M.D. Ziegler, J.P. Biersack, SRIM – the stopping and range of ions in matter, *Nucl. Instr. Meth. B* 268 (2010) 1818.
- [34] A.P. Hammersley, S.O. Svensson, M. Hanfland, A.N. Fitch, D. Häussermann, Two-dimensional detector software: from real detector to idealized image or two-theta scan, *High Press. Res.* 14 (1996) 235–248.
- [35] M. Lang, F.X. Zhang, F.X. Li, D. Severin, M. Bender, S. Klumünzer, C. Trautmann, R.C. Ewing, Swift heavy ion-induced amorphization of  $\text{CaZrO}_3$  perovskite, *Nucl. Instr. Meth. B* 286 (2012) 271–276.
- [36] W.J. Weber, Models and mechanisms of irradiation-induced amorphization in ceramics, *Nucl. Instr. Meth. B* 166–167 (2000) 98–106.
- [37] B.D. Begg, N.J. Hess, D.E. McCready, S. Thevuthasan, W.J. Weber, Heavy-ion irradiation effects in  $\text{Gd}_2(\text{Ti}_{2-x}\text{Zr}_x)\text{O}_7$  pyrochlores, *J. Nucl. Mater.* 289 (2001) 188–193.
- [38] N.J. Hess, B.D. Begg, S.D. Conradson, D.E. McCready, P.L. Gassmann, W.J. Weber, Spectroscopic investigations of the structural phase transition in  $\text{Gd}_2(\text{Ti}_{1-y}\text{Zr}_y)_2\text{O}_7$  pyrochlores, *J. Phys. Chem. B* 106 (2002) 4663–4677.
- [39] A. Meftah, F. Brisard, J.M. Costantini, M. Hage-Ali, J.P. Stoquert, F. Studer, M. Toulemonde, Swift heavy ions in magnetic insulators: a damage-cross-section velocity effect, *Phys. Rev. B* 48 (1993) 920–925.
- [40] W.J. Weber, N.J. Hess, G.D. Maupin, Amorphization in  $\text{Gd}_2\text{Ti}_2\text{O}_7$  and  $\text{CaZrTi}_2\text{O}_7$  irradiated with 3 MeV argon ions, *Nucl. Instr. Meth. B* 65 (1992) 102–106.
- [41] G. Szenes, General features of latent track formation in magnetic insulators irradiated with swift heavy ions, *Phys. Rev. B* 51 (1995) 8026–8029.
- [42] M. Toulemonde, G. Fuchs, N. Nguyen, F. Studer, D. Groult, Damage processes and magnetic field orientation in ferrimagnetic oxides  $\text{Y}_3\text{Fe}_5\text{O}_{12}$  and  $\text{BaFe}_{12}\text{O}_{19}$  irradiated by high-energy heavy ions: a Mössbauer study, *Phys. Rev. B* 35 (1987) 6560–6569.
- [43] J. Lian, L.M. Wang, S.X. Wang, J. Chen, L.A. Boatner, R.C. Ewing, Nanoscale manipulation of pyrochlore: new nanocomposite ionic conductors, *Phys. Rev. Lett.* 87 (2001) 145901.
- [44] M. Lang, F.X. Zhang, J.M. Zhang, J.W. Wang, B. Schuster, C. Trautmann, R. Neumann, U. Becker, R.C. Ewing, Nanoscale manipulation of the properties of solids at high pressure with relativistic heavy ions, *Nat. Mater.* 8 (2009) 793–797.
- [45] A.A. Gribb, J.F. Banfield, Particle size effects on transformation kinetics and phase stability in nanocrystalline  $\text{TiO}_2$ , *Am. Mineral.* 82 (1997) 717–728.
- [46] W.C. Jung, J.L. Hertz, H.L. Tuller, Enhanced ionic conductivity and phase metastability of nano-sized thin film yttria-doped zirconia (YDZ), *Acta Mater.* 57 (2009) 1399–1404.
- [47] R.L. Fleischer, P.B. Price, R.M. Walker, *Nuclear Tracks in Solids: Principles and Applications*, Univ. of California Press, 1975.
- [48] L.T. Chadderton, I. McC. Torrens, *Fission Damage in Crystals*, Methuen & Co. Ltd, 1969.
- [49] F. Seitz, J.S. Koehler, Displacement of atoms during irradiation, *Solid State Phys.* 2 (1956) 305–448.
- [50] B. Canut, N. Bonardi, S.M.M. Ramos, S. Della-Negra, Latent tracks formation in silicon single crystals irradiated with fullerenes in the electronic regime, *Nucl. Instr. Meth. B* 146 (1998) 296–301.
- [51] P.I. Gaiduk, L.A. Nylandsted, C. Trautmann, M. Toulemonde, Discontinuous tracks in arsenic-doped crystalline  $\text{Si}_{0.5}\text{Ge}_{0.5}$  alloy layers, *Phys. Rev. B* 66 (2002) 045316.
- [52] A. Colder, O. Marty, B. Canut, M. Levalois, P. Marie, X. Portier, S.M.M. Ramos, M. Toulemonde, Latent track formation in germanium irradiated with 20, 30 and 40 MeV fullerenes in the electronic regime, *Nucl. Instr. Meth. B* 174 (2001) 491–498.
- [53] C. Dufour, A. Audouard, F. Beuneu, J. Dural, J.P. Girard, A. Hairie, M. Levalois, E. Paumier, M. Toulemonde, A high-resistivity phase induced by swift heavy-ion irradiation of Bi: a probe for thermal spike damage?, *J. Phys. Condens. Matter* 5 (1993) 4573–4584.
- [54] A. Dunlop, D. Lesueur, P. Legrand, H. Dammak, J. Dural, Effects induced by high electronic excitations in pure metals: a detailed study in iron, *Nucl. Instr. Meth. B* 90 (1994) 330–338.
- [55] S. Klumünzer, M.-D. Hou, S. Schumacher, Coulomb explosions in a metallic glass due to the passage of fast heavy ions, *Phys. Rev. Lett.* 57 (1986) 850–853.
- [56] A. Audouard, E. Balanzat, G. Fuchs, J.C. Jousset, D. Lesueur, L. Thomé, High-energy heavy-ion irradiations of  $\text{Fe}_{85}\text{B}_{15}$  amorphous alloy: evidence for electronic energy loss effect, *Europhys. Lett.* 3 (1987) 327–331.
- [57] Z.G. Wang, C. Dufour, E. Paumier, M. Toulemonde, The  $S_p$  sensitivity of metals under swift-heavy-ion irradiation: a transient thermal process, *J. Phys. Condens. Matter* 6 (1995) 6733–6750 (*J. Phys. Condens. Matter* 7 2525–2526).
- [58] A. Chettah, H. Kucal, Z.G. Wang, M. Kac, A. Meftah, M. Toulemonde, Behavior of crystalline silicon under huge electronic excitations: a transient thermal spike description, *Nucl. Instr. Meth. B* 267 (2009) 2719–2724.
- [59] A. Kamarou, W. Wesch, E. Wendler, A. Undisz, M. Rettenmayr, Radiation damage formation in InP, InSb, GaAs, GaP, Ge, and Si due to fast ions, *Phys. Rev. B* 78 (2008) 054111.
- [60] M. Toulemonde, C. Dufour, A. Meftah, E. Paumier, Transient thermal processes in heavy ion irradiation of crystalline inorganic insulators, *Nucl. Instr. Meth. B* 166–167 (2000) 903–912.
- [61] H.D. Mieskes, W. Assmann, F. Gruener, H. Kucal, Z.G. Wang, M. Toulemonde, Electronic and nuclear thermal spike effects in sputtering of metals with energetic heavy ions, *Phys. Rev. B* 67 (2003) 155414.
- [62] M. Toulemonde, W. Assmann, F. Grüner, C. Trautmann, Jetlike component in sputtering of LiF induced by swift heavy ions, *Phys. Rev. Lett.* 88 (2002) 057602.
- [63] M. Toulemonde, A. Benyagoub, C. Trautmann, N. Khalfaoui, M. Boccanfuso, C. Dufour, F. Goubilleau, J.J. Grob, J.P. Stoquert, J.M. Costantini, F. Haas, E. Jacquet, K.-O. Voss, A. Meftah, Dense and nanometric electronic excitations induced by swift heavy ions in an ionic  $\text{CaF}_2$  crystal: evidence for two thresholds of damage creation, *Phys. Rev. B* 85 (2012) 054112.
- [64] E.M. Bringa, R.E. Johnson, Coulomb explosion and thermal spikes, *Phys. Rev. Lett.* 88 (2002) 165501.
- [65] M. Toulemonde, C. Trautmann, E. Balanzat, K. Hjort, A. Weidinger, Track formation and fabrication of nanostructures with MeV-ion beams, *Nucl. Instr. Meth. B* 216 (2004) 1–8.

- [66] I.M. Lifshitz, M.I. Kaganov, L.V. Taratanov, On the theory of radiation-induced changes in metals, *J. Nucl. Energy A* 12 (1960) 69–78.
- [67] C. Zhang, D.E. Dunn, R. Katz, Radial distribution of dose and cross-sections for the inactivation of dry enzymes and viruses, *Radiat. Prot. Dosim.* 13 (1985) 215–218.
- [68] M.P.R. Waligorski, R.N. Hamm, R. Katz, The radial distribution of dose around the path of a heavy ion in liquid water, *Nucl. Tracks Radiat. Meas.* 11 (1986) 309–319.
- [69] B. Gervais, S. Bouffard, Simulation of the primary stage of the interaction of swift heavy ions with condensed matter, *Nucl. Instr. Meth. B* 88 (1994) 355–364.
- [70] J. Chen, J. Lian, L.M. Wang, R.C. Ewing, J.M. Farmer, L.A. Boatner, in: *Scientific Basis for Nuclear Waste Management XXV*, MRS Symposia Proceedings No. 713 Materials Research Society, Warrendale, 1998, p. 501.
- [71] P.J. Wilde, C.R.A. Catlow, Defects and diffusion in pyrochlore structured oxides, *Solid State Ionics* 112 (1998) 173–183.
- [72] I. Jozwik-Biala, J. Jagielski, B. Arey, L. Kovarik, G. Sattonnay, A. Debelle, S. Mylonas, I. Monnet, L. Thomé, Effect of combined local variations in elastic and inelastic energy losses on the morphology of tracks in ion-irradiated materials, *Acta Mater.* 61 (2013) 4669–4675.
- [73] A.V. Radha, S.V. Ushakov, A. Navrotsky, Thermochemistry of lanthanum zirconate pyrochlore, *J. Mater. Res.* 24 (2009) 3350–3357.